The Spatial Distribution of Globular Cluster Systems in Early-type Galaxies: Estimation Procedure and Catalog of Properties for Globular Cluster Systems Observed with Deep Imaging Surveys

Sungsoon Lim, Eric W Peng, Patrick Côté, Laura Ferrarese, Joel C Roediger, Chengze Liu, Chelsea Spengler, Elisabeth Sola, Pierre-Alain Duc, Laura V Sales, et al.

The Astrophysical Journal Supplement Series, 276:34 (20pp), 2025 February https://doi.org/10.3847/1538-4365/ad97b7

The Spatial Distribution of Globular Cluster Systems in Early-type Galaxies: Estimation Procedure and Catalog of Properties for Globular Cluster Systems Observed with Deep Imaging Surveys

Sungsoon Lim[1], Eric W. Peng[2], Patrick Côté[3], Laura Ferrarese[3], Joel C. Roediger[3], Chengze Liu[4], Chelsea Spengler[5], Elisabeth Sola[6], Pierre-Alain Duc[7], Laura V. Sales[8], John P. Blakeslee[2], Jean-Charles Cuillandre[9], Patrick R. Durrell[10], Eric Emsellem[11], Stephen D. J. Gwyn[3], Ariane Lançon[7], Francine R. Marleau[12], J. Christopher Mihos[13], Oliver Müller[14], Thomas H. Puzia[5], and Rubén Sánchez-Janssen[15]
[1] Department of Astronomy, Yonsei University, 50 Yonsei-ro, Seodaemun-gu, Seoul 03722, Republic of Korea; sslim00@gmail.com
[2] NSF's NOIRLab, 950 N. Cherry Avenue, Tucson, AZ 85719, USA
[3] Herzberg Astronomy and Astrophysics Research Centre, National Research Council of Canada, Victoria, BC V9E 2E7, Canada
[4] Department of Astronomy, School of Physics and Astronomy, and Shanghai Key Laboratory for Particle Physics and Cosmology, Shanghai Jiao Tong University, Shanghai 200240, People's Republic of China
[5] Institute of Astrophysics, Pontificia Universidad Católica de Chile, Av. Vicuña Mackenna 4860, 7820436 Macul, Santiago, Chile
[6] Institute of Astronomy, Madingley Road, Cambridge, CB3 0HA, UK
[7] Université de Strasbourg, CNRS, Observatoire astronomique de Strasbourg (ObAS), UMR 7550, 67000 Strasbourg, France
[8] Department of Physics and Astronomy, University of California, Riverside, 900 University Avenue, Riverside, CA 92521, USA
[9] AIM Paris Saclay, CNRS/INSU, CEA/Irfu, Université Paris Diderot, Orme des Merisiers, F-91191 Gif-sur-Yvette Cedex, France
[10] Department of Physics and Astronomy, Youngstown State University, One University Plaza, Youngstown, OH 44555, USA
[11] European Southern Observatory, Karl-Schwarzschild Straße 2, D-85748 Garching bei München, Germany
[12] Institut für Astro- und Teilchenphysik, Universität Innsbruck, Technikerstraße 25/8, Innsbruck, A-6020, Austria
[13] Department of Astronomy, Case Western Reserve University, Cleveland, OH 44106, USA
[14] Institute of Physics, Laboratory of Astrophysics, École Polytechnique Fédérale de Lausanne (EPFL), 1290 Sauverny, Switzerland
[15] STFC UK Astronomy Technology Centre, Royal Observatory, Blackford Hill, Edinburgh, EH9 3HJ, UK
Received 2024 June 2; revised 2024 November 6; accepted 2024 November 24; published 2025 January 14

Abstract

We present an analysis of the spatial distribution of globular cluster (GC) systems of 118 nearby early-type galaxies in the Next Generation Virgo Cluster Survey and Mass Assembly of early-Type GaLAxies with their fine Structures survey programs, which both used MegaCam on the Canada–France–Hawaii Telescope. We describe the procedure used to select GC candidates and fit the spatial distributions of GCs to a two-dimensional Sérsic function, which provides effective radii (half number radii) and Sérsic indices, and estimate background contamination by adding a constant term to the Sérsic function. In cases where a neighboring galaxy affects the estimation of the GC spatial distribution in the target galaxy, we fit two two-dimensional Sérsic functions, simultaneously. We also investigate the color distributions of GCs in our sample by using Gaussian mixture modeling. For GC systems with bimodal color distributions, we divide the GCs into blue and red subgroups and fit their respective spatial distributions with Sérsic functions. Finally, we measure the total number of GCs based on our fitted Sérsic function, and calculate the GC specific frequency.

Unified Astronomy Thesaurus concepts: Early-type galaxies (429); Virgo Cluster (1772); Globular star clusters (656); Field galaxies (533); Galaxy evolution (594)

Materials only available in the online version of record: figure sets

1. Introduction

Globular clusters (GCs) have long been used as probes of galaxy formation and evolution. While studies of GCs belonging to individual galaxies have provided many insights into galaxy evolution, it is the systematic study of GCs in large surveys (e.g., P. Côté et al. 2004; J. P. Jordán et al. 2007a; B. W. Miller & J. M. Lotz 2007; I. Y. Georgiev et al. 2009; K. L. Rhode 2012; J. P. Brodie et al. 2014; D. Zaritsky et al. 2015; K. A. Alamo-Martìnez et al. 2021) that allows us to explore the general relationships between GC systems and their host galaxies. For example, it is well known that GC color distributions and total numbers (or total masses) are closely related to properties of their host galaxies (e.g., J. P. Blakeslee et al. 1997; E. W. Peng et al. 2006, 2008; L. R. Spitler & D. A. Forbes 2009; W. E. Harris et al. 2017). Although GC colors and numbers have been used to study galaxy formation and evolution with empirical relations (e.g., M. G. Lee et al. 2010; A. L. Chies-Santos et al. 2011; E. W. Peng et al. 2011; S. Lim & E. W. Peng 2018; D. J. Prole et al. 2019; S. Lim et al. 2020; K. Hartman et al. 2023; W. E. Harris 2023), much less is known about the spatial distribution of GC systems as this requires deep, wide-field imaging from galaxy cores to their peripheries.

Early efforts focused on estimating GC "spatial extents," taken to be the point where the GC number density profile merges into the background (e.g., K. L. Rhode et al. 2007; J. R. Hargis & K. L. Rhode 2012, 2014). While this concept of "GC extent" can be helpful in understanding how far GCs extend from the galaxy center, a homogeneous comparison of results from different surveys can be problematic.

For this reason, functional modeling of GC spatial distributions is generally needed to avoid dependence on surveys.

There have been wide-field imaging surveys for GCs in individual, or handfuls, of galaxies that estimated effective radii for GC systems (e.g., C. Blom et al. 2012; C. Usher et al. 2013; W. E. Harris et al. 2014; S. S. Kartha et al. 2014, 2016), but sample sizes have been too small to fully explore the link between galaxy properties and GC system size. Several recent studies have reported effective radii for GC systems (and other galaxy properties), but there are often discrepancies among the results; moreover, samples have been still limited to 20–30 galaxies—usually massive systems (D. A. Forbes 2017; M. J. Hudson & B. Robison 2018; J. P. Caso et al. 2019). A few studies estimating GC spatial distributions with functional models for a large sample of galaxies exist (e.g., D. Zaritsky et al. 2015; K. A. Alamo-Martìnez & J. P. Blakeslee 2017), but they have not focused on the spatial distributions of GC systems. Therefore, a systematic study of GC spatial distributions for a larger, more representative sample of galaxies is needed to better understand GC spatial distributions.

In this study, we examine the spatial distribution of GCs belonging to 118 early-type galaxies (ETGs) based on imaging from two large nearby galaxy surveys—the Next Generation Virgo Cluster Survey (NGVS; PI: Ferrarese, L., L. Ferrarese et al. 2012) and Mass Assembly of early-Type GaLAxies with their fine Structures (MATLAS; PI: Duc, P.-A., P.-A. Duc 2020). Additionally, our analysis also uses Hubble Space Telescope (HST) imaging from the Advanced Camera for Surveys (ACS) Virgo Cluster Survey (PI: Cote, P.). We note that the scientific analysis and interpretation of the results are published in S. Lim et al. (2024), so the focus of this paper is on the data products. In Section 2, we describe our data and methods, including photometry and fitting for analytic functional form. In Section 3, the results of individual galaxies are presented and discussed. We summarize our results in Section 4.

2. Data and Methodology

2.1. Target Selection

The data used in this study were obtained from two large optical imaging surveys: NGVS and MATLAS. While imaging for numerous galaxies is available from these surveys, we limited our targets to ensure reliable GC studies, mainly focusing on ETGs. First, we targeted nearby ($\leqslant$25 Mpc) MATLAS galaxies (including galaxies inside the NGVS footprint) that were observed in at least three filters. Second, we also targeted ACSVCS galaxies inside the NGVS footprint to include low-mass (early-type dwarf) galaxies in our sample. Among the galaxies that satisfy the above categories, several systems were too close to neighboring, giant galaxies with their own rich GC systems, making it almost impossible to detect and study GCs in these galaxies; such objects were excluded for our analysis. Ultimately, we targeted 118 galaxies in this study. Table 1 lists our targets and their properties.

2.2. The Next Generation Virgo Cluster Survey

The NGVS is a deep, multiband imaging survey of the Virgo cluster carried out with MegaCam (O. Boulade et al. 2003) on the Canada–France–Hawaii Telescope (CFHT) from 2008 to 2013. The survey covers an area of 104 deg^2 (with 117 pointings) within the virial radii of both the Virgo A and Virgo B subclusters. Full survey details, including observing strategy and data processing, are described in L. Ferrarese et al. (2012). Additional details on the data reduction and analysis procedures are also available in L. Ferrarese et al. (2020).

2.3. The Mass Assembly of Early-type Galaxies with Their Fine Structures

The MATLAS survey is a second deep imaging survey using MegaCam on CFHT. The targets of the MATLAS survey are galaxies from the ATLAS^{3D} sample (M. Cappellari et al. 2011). The sample contains 260 nearby (within 42 Mpc) bright ($M_K < -21.5$) ETGs. Full survey details are available in P.-A. Duc et al. (2015), P.-A. Duc (2020), and M. Bìlek et al. (2020), and the data reduction process is described in S. D. J. Gwyn (2008).

2.4. Photometry

We used the NGVS aperture photometry catalog for the NGVS samples. The catalog details are fully described in C. Liu et al. (2015), so we present here only a brief description of the catalog. SExtractor (E. Bertin & S. Arnouts 1996) was run on the processed images to obtain aperture magnitudes of sources with dual-image mode. We used the g'-band images as detection images and adopted circular apertures with a series of diameters between 2 and 16 pixels to measure the source fluxes, which were then corrected to 16 pixel diameter aperture magnitudes. Instrumental magnitudes were then calibrated to standard AB magnitudes through a comparison to SDSS point-spread function (PSF) magnitudes after a conversion to MegaCam filter magnitudes.

The central regions of some galaxies have high surface brightness, making it difficult to estimate the background and detect sources with general photometry programs such as SExtractor. Since all NGVS galaxies have been modeled with customized two-dimensional isophote (ISO) fitting models (L. Ferrarese et al. 2020), we subtracted diffuse light from galaxies using ISO fit models to enhance source detection and background estimation. The model subtraction is performed with cutout images having a $10' \times 10'$ field of view (FoV). We then ran SExtractor on these galaxy-subtracted images in the same way as for the NGVS source catalog. The magnitudes measured on the model-subtracted images are then matched with the original NGVS catalog by comparing magnitudes of sources in the outer $2'$ width area of model-subtracted images. We replaced the NGVS aperture photometry catalogs of the central $8' \times 8'$ regions of our target galaxies with the photometric catalogs on the model-subtracted images.

We also generated aperture photometry catalogs for MATLAS galaxies using the same methodology as the NGVS aperture photometry catalog. However, the detection images and galaxy model subtraction for MATLAS galaxies differ slightly from those for NGVS galaxies. For the detection image, we chose the best seeing filter image for MATLAS. We used ring-median-filtered galaxy models instead of two-dimensional ISO fit models for the model subtraction. The ring-median filtering method can produce diffuse images by setting the inner and outer ring sizes. We set the radii of the inner and outer rings to 15 and 20 pixels, respectively. We subtracted these ring-median-filtered model galaxies from the MATLAS cutout images with an FoV of $10' \times 10'$, similar to the NGVS data. Additionally, we replaced the MATLAS aperture photometry catalogs for the central $8' \times 8'$ regions of our target galaxies with photometric catalogs based on the model-subtracted images.

Table 1
List of Sample Galaxies

Name	R.A. (J2000) (deg)	Decl. (J2000) (deg)	M_g (mag)	$(g' - i')_0$ (mag)	M_* ($M_\odot$)	$R_{e,*}$ (arcsec)	Distance (Mpc)	Survey	Other Name
(1)	(2)	(3)	(4)	(5)	(6)	(7)	(8)	(9)	(10)
NGC 0524	21.198778	9.538793	−20.82	1.00	1.2×10^{11}	43.7	23.3	MATLAS	...
NGC 0821	32.088123	10.994870	−20.62	0.81	7.9×10^{10}	39.8	23.4	MATLAS	...
NGC 0936	36.906090	−1.156280	−21.16	1.01	9.8×10^{10}	52.5	22.4	MATLAS	...
NGC 1023	40.100052	39.063251	−20.20	0.96	5.1×10^{10}	47.9	11.1	MATLAS	...
NGC 2592	126.783669	25.970339	−19.07	1.03	3.7×10^{10}	12.3	25.0	MATLAS	...
NGC 2685	133.894791	58.734409	−19.18	0.80	1.2×10^{10}	25.7	16.7	MATLAS	...
NGC 2768	137.906265	60.037209	−20.91	1.03	2.7×10^{11}	63.1	21.8	MATLAS	...
NGC 2778	138.101639	35.027424	−18.73	0.92	2.4×10^{10}	15.8	22.3	MATLAS	...
NGC 2950	145.646317	58.851219	−19.43	0.93	2.1×10^{10}	15.5	14.5	MATLAS	...
NGC 3098	150.569458	24.711092	−19.23	0.91	1.7×10^{10}	13.2	23.0	MATLAS	...
NGC 3245	156.826523	28.507435	−20.09	0.92	4.5×10^{10}	25.1	20.3	MATLAS	...
NGC 3379	161.956665	12.581630	−20.07	1.04	5.0×10^{10}	39.8	10.3	MATLAS	M105
NGC 3384	162.070404	12.629300	−19.89	0.93	2.4×10^{10}	32.4	11.3	MATLAS	...
NGC 3457	163.702591	17.621157	−18.56	0.88	4.0×10^{9}	13.5	20.1	MATLAS	...
NGC 3489	165.077454	13.901258	−19.60	0.85	8.6×10^{9}	22.4	11.7	MATLAS	...
NGC 3599	168.862305	18.110369	−19.02	0.88	7.2×10^{9}	23.4	19.8	MATLAS	...
NGC 3607	169.227737	18.051809	−21.19	0.96	1.6×10^{11}	38.9	22.2	MATLAS	...
NGC 3608	169.245697	18.148531	−19.99	0.96	6.4×10^{10}	29.5	19.8	MATLAS	...
NGC 3630	170.070786	2.964170	−19.55	0.95	2.5×10^{10}	12.6	25.0	MATLAS	...
NGC 3945	178.307190	60.675560	−20.72	1.03	6.9×10^{10}	28.2	23.2	MATLAS	...
IC 3032	182.782333	14.274944	−15.96	0.77	6.3×10^{8}	9.0	15.0	NGVS,ACSVCS	VCC 33
IC 3065	183.802417	14.433083	−17.11	0.83	2.0×10^{9}	9.2	16.5	NGVS,ACSVCS	VCC 140
VCC 200	184.140333	13.031417	−16.70	0.86	5.9×10^{8}	12.9	18.3	NGVS,ACSVCS	...
IC 3101	184.331833	11.943389	−15.92	0.86	4.4×10^{8}	9.4	17.9	NGVS,ACSVCS	VCC 230
NGC 4262	184.877426	14.877717	−19.00	1.04	1.9×10^{10}	8.5	15.5	NGVS,ACSVCS	VCC 355
NGC 4267	184.938675	12.798356	−19.66	1.06	3.9×10^{10}	28.9	15.8	NGVS,ACSVCS	VCC 369
NGC 4278	185.028320	29.280619	−20.16	1.02	7.5×10^{10}	31.6	15.6	MATLAS	...
NGC 4283	185.086609	29.310898	−18.21	1.02	8.3×10^{9}	12.3	15.3	MATLAS	...
UGC 7436	185.581458	14.760722	−17.00	0.84	2.1×10^{9}	18.2	15.8	NGVS,ACSVCS	VCC 543
VCC 571	185.671417	7.950306	−17.02	0.80	6.3×10^{8}	10.6	23.8	NGVS,ACSVCS	...
NGC 4318	185.680458	8.198250	−18.05	0.95	3.3×10^{9}	5.8	22.0	NGVS,ACSVCS	VCC 575
NGC 4339	185.895599	6.081713	−19.18	1.03	1.9×10^{10}	24.8	16.0	NGVS	VCC 648
NGC 4340	185.897141	16.722195	−19.70	1.01	2.3×10^{10}	29.0	18.4	NGVS,ACSVCS	VCC 654
NGC 4342	185.912598	7.053936	−18.52	1.15	1.2×10^{10}	4.5	16.5	NGVS	VCC 657
NGC 4350	185.990891	16.693356	−19.69	1.08	3.4×10^{10}	15.1	15.4	NGVS,ACSVCS	VCC 685
NGC 4352	186.020833	11.218333	−18.42	0.96	6.2×10^{9}	15.6	18.5	NGVS,ACSVCS	VCC 698
NGC 4365	186.117615	7.317520	−22.02	1.04	1.3×10^{11}	75.4	23.1	NGVS,ACSVCS	VCC 731
NGC 4371	186.230957	11.704288	−19.99	1.05	3.9×10^{10}	28.5	16.9	NGVS,ACSVCS	VCC 759
NGC 4374	186.265747	12.886960	−22.05	1.06	2.2×10^{11}	90.4	18.5	NGVS,ACSVCS	M84, VCC 763
NGC 4377	186.301285	14.762218	−19.04	0.99	1.5×10^{10}	10.7	17.7	NGVS,ACSVCS	VCC 778
NGC 4379	186.311386	15.607498	−18.89	1.01	1.6×10^{10}	13.7	15.9	NGVS,ACSVCS	VCC 784
NGC 4387	186.423813	12.810359	−18.72	1.02	1.1×10^{10}	10.8	18.0	NGVS,ACSVCS	VCC 828
IC 3328	186.490875	10.053556	−17.21	0.86	2.1×10^{9}	17.4	16.9	NGVS,ACSVCS	VCC 856
NGC 4406	186.549225	12.945970	−22.24	1.00	2.6×10^{11}	135.8	17.9	NGVS,ACSVCS	M86, VCC 881
NGC 4417	186.710938	9.584117	−19.50	1.01	2.5×10^{10}	15.3	16.0	NGVS,ACSVCS	VCC 944
NGC 4425	186.805664	12.734803	−18.77	1.02	1.3×10^{10}	16.9	16.5	NGVS	VCC 984
NGC 4429	186.860657	11.107540	−20.72	1.08	8.8×10^{10}	42.8	16.5	NGVS	VCC 1003
NGC 4434	186.902832	8.154311	−19.32	0.98	1.1×10^{10}	12.1	22.5	NGVS,ACSVCS	VCC 1025
NGC 4435	186.918762	13.079021	−20.15	1.03	4.3×10^{10}	25.6	16.7	NGVS,ACSVCS	VCC 1030
NGC 4442	187.016220	9.803620	−20.04	1.07	5.2×10^{10}	17.8	15.3	NGVS,ACSVCS	VCC 1062
IC 3383	187.051208	10.297500	−16.41	0.87	9.3×10^{8}	18.6	16.2	NGVS,ACSVCS	VCC 1075
IC 3381	187.062083	11.790000	−18.06	0.88	4.2×10^{9}	40.4	16.7	NGVS,ACSVCS	VCC 1087
NGC 4452	187.180417	11.755000	−18.43	0.95	9.0×10^{9}	15.1	15.6	NGVS,ACSVCS	VCC 1125
NGC 4458	187.239716	13.241916	−18.76	0.96	1.0×10^{10}	21.9	16.3	NGVS,ACSVCS	VCC 1146
NGC 4459	187.250107	13.978580	−20.47	1.03	7.2×10^{10}	41.0	16.0	NGVS,ACSVCS	VCC 1154
NGC 4461	187.262543	13.183857	−19.59	1.03	2.9×10^{10}	18.6	16.5	NGVS	VCC 1158
VCC 1185	187.347625	12.450667	−16.05	0.87	7.6×10^{8}	19.4	16.9	NGVS,ACSVCS	...
NGC 4472	187.444992	8.000410	−22.65	1.02	3.7×10^{11}	225.6	16.7	NGVS,ACSVCS	M49, VCC 1226
NGC 4473	187.453659	13.429320	−20.42	1.02	5.7×10^{10}	32.9	15.2	NGVS,ACSVCS	VCC 1231
NGC 4474	187.473099	14.068673	−19.03	0.94	1.4×10^{10}	20.0	15.5	NGVS,ACSVCS	VCC 1242
NGC 4476	187.496170	12.348669	−18.82	0.91	7.3×10^{9}	18.1	17.7	NGVS,ACSVCS	VCC 1250
NGC 4477	187.509048	13.636443	−20.25	1.06	5.5×10^{10}	33.7	16.5	NGVS	VCC 1253
NGC 4482	187.543292	10.779472	−18.10	0.85	4.1×10^{9}	20.1	18.2	NGVS,ACSVCS	VCC 1261

Table 1
(Continued)

Name	R.A. (J2000) (deg)	Decl. (J2000) (deg)	M_g (mag)	$(g' - i')_0$ (mag)	M_* ($M_\odot$)	$R_{e,*}$ (arcsec)	Distance (Mpc)	Survey	Other Name
(1)	(2)	(3)	(4)	(5)	(6)	(7)	(8)	(9)	(10)
NGC 4478	187.572662	12.328578	−19.40	1.01	1.4×10^{10}	12.3	17.1	NGVS,ACSVCS	VCC 1279
NGC 4479	187.576667	13.578028	−18.24	1.01	7.2×10^{9}	17.6	17.4	NGVS,ACSVCS	VCC 1283
NGC 4483	187.669250	9.015665	−18.46	0.98	7.5×10^{9}	12.6	16.7	NGVS,ACSVCS	VCC 1303
NGC 4486	187.705933	12.391100	−22.23	1.01	2.9×10^{11}	105.0	16.7	NGVS,ACSVCS	M87, VCC 1316
NGC 4489	187.717667	16.758696	−18.39	0.92	8.7×10^{9}	17.8	15.4	NGVS,ACSVCS	VCC 1321
IC 3461	188.011208	11.890222	−16.36	0.89	1.1×10^{9}	11.6	16.8	NGVS,ACSVCS	VCC 1407
NGC 4503	188.025803	11.176434	−19.58	1.06	3.3×10^{10}	21.7	16.5	NGVS	VCC 1412
IC 3468	188.059208	10.251389	−17.79	0.86	3.5×10^{9}	29.2	15.4	NGVS,ACSVCS	VCC 1422
IC 3470	188.097375	11.262833	−16.90	0.97	2.3×10^{9}	10.1	16.0	NGVS,ACSVCS	VCC 1431
IC 798	188.139125	15.415333	−16.55	0.88	9.8×10^{8}	8.6	16.1	NGVS,ACSVCS	VCC 1440
NGC 4515	188.270625	16.265528	−18.16	0.91	5.5×10^{9}	9.7	16.7	NGVS,ACSVCS	VCC 1475
VCC 1512	188.394000	11.261889	−15.95	0.80	3.0×10^{8}	12.9	18.3	NGVS,ACSVCS	...
IC 3501	188.465083	13.322583	−16.81	0.92	1.7×10^{9}	10.1	16.3	NGVS,ACSVCS	VCC 1528
NGC 4528	188.525269	11.321266	−18.59	1.02	1.2×10^{10}	8.9	15.7	NGVS,ACSVCS	VCC 1537
VCC 1539	188.528208	12.741694	−15.48	1.00	4.1×10^{8}	17.1	17.0	NGVS,ACSVCS	...
IC 3509	188.548083	12.048861	−16.32	1.06	1.1×10^{9}	9.9	16.8	NGVS,ACSVCS	VCC 1545
NGC 4550	188.877548	12.220955	−18.89	1.03	1.6×10^{10}	11.4	15.3	NGVS,ACSVCS	VCC 1619
NGC 4551	188.908249	12.264010	−18.70	1.04	1.4×10^{10}	13.8	16.2	NGVS,ACSVCS	VCC 1630
NGC 4552	188.916183	12.556040	−21.07	1.03	9.6×10^{10}	59.2	16.0	NGVS,ACSVCS	M89, VCC 1632
VCC 1661	189.103375	10.384611	−15.40	0.90	5.3×10^{8}	18.7	15.8	NGVS,ACSVCS	...
NGC 4564	189.112473	11.439320	−19.55	1.01	2.3×10^{10}	16.4	15.9	NGVS,ACSVCS	VCC 1664
NGC 4570	189.222504	7.246663	−19.95	1.04	3.5×10^{10}	14.5	17.1	NGVS,ACSVCS	VCC 1692
NGC 4578	189.377274	9.555121	−19.28	0.96	1.9×10^{10}	25.6	16.4	NGVS,ACSVCS	VCC 1720
NGC 4596	189.983063	10.176031	−20.46	1.00	5.0×10^{10}	42.3	16.5	NGVS	VCC 1813
VCC 1826	190.046833	9.896083	−15.61	0.87	5.3×10^{8}	6.6	16.3	NGVS,ACSVCS	...
VCC 1833	190.081875	15.935333	−16.76	0.83	1.5×10^{9}	7.8	16.3	NGVS,ACSVCS	...
IC 3647	190.221250	10.476111	−16.91	0.60	2.0×10^{8}	37.7	16.2	NGVS,ACSVCS	VCC 1857
IC 3652	190.243917	11.184556	−17.19	0.91	2.4×10^{9}	20.3	16.1	NGVS,ACSVCS	VCC 1861
NGC 4608	190.305374	10.155793	−19.71	0.96	3.0×10^{10}	26.6	16.5	NGVS	VCC 1869
IC 3653	190.315500	11.387083	−16.98	0.97	2.6×10^{9}	7.0	15.5	NGVS,ACSVCS	VCC 1871
NGC 4612	190.386490	7.314782	−19.50	0.91	1.6×10^{10}	25.1	16.5	NGVS,ACSVCS	VCC 1883
VCC 1886	190.414208	12.247889	−15.89	0.69	2.1×10^{8}	14.1	15.7	NGVS,ACSVCS	...
UGC 7854	190.466667	9.402861	−16.24	0.83	8.4×10^{8}	10.3	15.9	NGVS,ACSVCS	VCC 1895
NGC 4621	190.509674	11.646930	−21.02	1.02	9.7×10^{10}	69.1	14.9	NGVS,ACSVCS	M59, VCC 1903
NGC 4638	190.697632	11.442459	−19.62	0.96	2.0×10^{10}	12.5	17.5	NGVS,ACSVCS	VCC 1938
NGC 4649	190.916702	11.552610	−21.99	1.06	2.5×10^{11}	76.0	16.5	NGVS,ACSVCS	M60, VCC 1978
VCC 1993	191.050083	12.941694	−15.87	0.85	6.2×10^{8}	11.1	16.6	NGVS,ACSVCS	...
NGC 4660	191.133209	11.190533	−19.32	1.02	2.5×10^{10}	10.8	15.0	NGVS,ACSVCS	VCC 2000
IC 3735	191.335083	13.692500	−16.98	0.83	1.5×10^{9}	16.6	17.2	NGVS,ACSVCS	VCC 2019
IC 3773	191.813833	10.203611	−17.07	0.85	2.7×10^{9}	14.1	13.5	NGVS,ACSVCS	VCC 2048
IC 3779	191.836208	12.166306	−16.03	0.84	8.3×10^{8}	11.3	15.8	NGVS,ACSVCS	VCC 2050
NGC 4694	192.062881	10.983624	−19.39	0.72	8.1×10^{9}	25.6	16.5	NGVS	VCC 2066
NGC 4710	192.412323	15.165490	−19.94	0.99	4.5×10^{10}	25.2	16.5	NGVS	...
NGC 4733	192.778259	10.912103	−18.63	0.91	1.1×10^{10}	26.3	14.5	NGVS	VCC 2087
NGC 4754	193.073181	11.313660	−20.14	1.04	3.7×10^{10}	26.1	16.1	NGVS,ACSVCS	VCC 2092
NGC 4762	193.233536	11.230800	−20.93	1.02	7.1×10^{10}	31.9	22.6	NGVS,ACSVCS	VCC 2095
NGC 5839	226.364471	1.634633	−18.83	1.00	2.0×10^{10}	16.6	22.0	MATLAS	...
NGC 5846	226.621887	1.605637	−21.05	1.06	2.5×10^{11}	58.9	24.2	MATLAS	...
NGC 5866	226.623169	55.763309	−20.59	0.95	7.8×10^{10}	36.3	14.9	MATLAS	...
PGC 058114	246.517838	2.906550	−18.29	0.78	6.3×10^{9}	9.3	23.8	MATLAS	...
NGC 6548	271.496826	18.587217	−19.59	1.00	4.6×10^{10}	22.4	22.4	MATLAS	...
NGC 7280	336.614899	16.148266	−19.26	0.92	1.4×10^{10}	21.4	23.7	MATLAS	...
NGC 7332	339.352173	23.798351	−20.28	0.86	2.4×10^{10}	17.4	22.4	MATLAS	...
NGC 7457	345.249725	30.144892	−18.93	0.89	7.4×10^{9}	36.3	12.9	MATLAS	...
NGC 7454	345.277130	16.388371	−19.10	0.96	2.9×10^{10}	25.7	23.2	MATLAS	...

Note. For MATLAS galaxies, magnitudes and colors (columns (4), (5)) are from Sola et al. (2022); galaxy stellar masses (column (6)) are taken from M. Cappellari et al. (2013); and effective radii (column (7)) are results of M. Cappellari et al. (2011). For NGVS galaxies, magnitudes, colors, and effective radii (columns (4), (5), (7)) are taken from L. Ferrarese et al. (2020); and galaxy stellar masses (column (6)) are from J. C. Roediger et al. (2024, in preparation). The distances (column (8)) are based on HST surface brightness fluctuation measurements for ACSVCS galaxies (S. Mei et al. 2007; J. P. Blakeslee & S. Mei 2009), while distances for MATLAS and NGVS (not in ACSVCS) galaxies are taken from M. Cappellari et al. (2011). Please note that there is a slight difference between the absolute g'-magnitudes of the NGVS samples and those presented in Figure 1 of S. Lim et al. (2024). In S. Lim et al. (2024), we employed model-fitted magnitudes; however, in this study, we have chosen for curve-of-growth magnitudes, which we consider to be a more comprehensive magnitude for estimating the fluxes of galaxies.

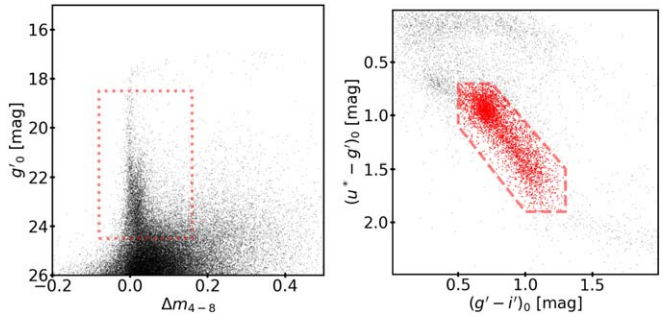

Figure 1. (Left) Inverse concentration index, Δm_{4-8}, vs. g-band magnitude for sources in the NGC 4472 region. The red dotted box shows the pointlike source region used for this galaxy. (Right) $(u^* - g')$-$(g' - i')$ color–color diagram of pointlike sources in the NGC 4472 region. The red dashed polygon shows the globular cluster (GC) selection region used in this study, with red sources showing GC candidates.

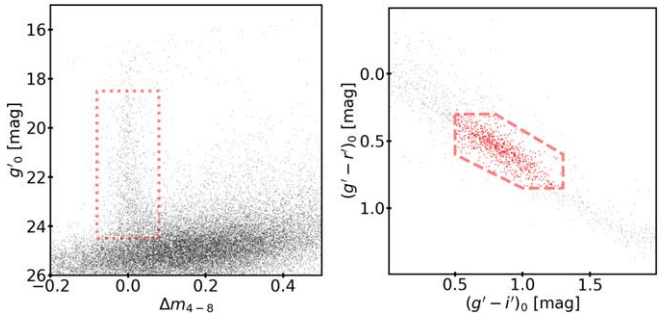

Figure 2. (Left) Inverse concentration index, Δm_{4-8}, vs. g-band magnitude for sources in the NGC 524 region. The red dotted box shows the pointlike source region used for this galaxy. (Right) $(g' - r')$-$(g' - i')$ color–color diagram of pointlike sources in the NGC 524 region. The red dashed polygon shows the GC selection region used in this study, with red sources showing GC candidates.

2.5. Globular Cluster Selection

We selected GC candidates based on a combination of size information and colors. Since most GCs at the distances of our target galaxies appear as pointlike, or slightly extended, sources in the images, we chose pointlike sources first based on the inverse concentration index, $\Delta m'_{4-8}$. This is the difference in magnitudes between apertures of 4 and 8 pixel diameters. These aperture magnitudes are corrected for missing point-source fluxes, so the $\Delta m'_{4-8}$ value of point sources is defined to be zero. We measured $\Delta m'_{4-8}$ values using the g'- and i'-band images for the NGVS targets and combined them with error-weighting. As for the MATLAS targets, we calculated Δm_{4-8} values on the best seeing filter image and the second best seeing images. These Δm_{4-8} values are also combined with error-weighting. We used these error-weighted mean Δm_{4-8} values for the point-source selection. The Δm_{4-8} values of point sources show scatter with a mean of zero due to photometric errors. Therefore, we chose pointlike sources with a range of Δm_{4-8} values, $-0.08 \leqslant \Delta m_{4-8} \leqslant 0.08$. We limited the selection to sources brighter than $g' = 24.5$ mag to mitigate the effect of large photometric errors. GCs at smaller galactocentric distances can be partially resolved in high-quality images, so we expanded the range of $\Delta m_{4\text{-}8}$ values as $-0.08 \leqslant \Delta m_{4-8} \leqslant 0.16$ for galaxies within 20 Mpc for the NGVS targets and for galaxies within 20 Mpc in MATLAS having high image quality (seeing $\leqslant 1.''0$). After selecting pointlike sources, we used color information to choose GCs. We chose GC candidates using polygons in the $(u^* - g') - (g' - i')$ color–color diagrams (Figure 1) when u-band data are available. Otherwise, we used $(g' - r') - (g' - i')$ color–color diagrams (Figure 2). All GC selection polygons are defined based on the M87 spectroscopically confirmed GCs (see S. Lim et al. 2017).

2.6. ACS Virgo Cluster Survey Data

Although model-subtracted images allow us to detect additional sources in the central regions of galaxies, the GC samples will still be incomplete in the cores of bright galaxies. Because we have targeted galaxies in the ACSVCS, we also have HST/ACS photometric catalogs that are much more complete than is possible with ground-based imaging. Our analysis thus uses the GC catalog from ACSVCS (A. Jordán et al. 2007b), which provides $g_{\rm ACS}$ and $z_{\rm ACS}$ magnitudes, and GC probability. We transformed these HST magnitudes to CFHT g and i magnitudes using the following linear equations derived from matched sources in the M87 region.

$$g'_{\rm NGV\,S} = g_{\rm ACS} - (0.060 \pm 0.005) - (0.057 \pm 0.004) \times (g_{\rm ACS} - z_{\rm ACS}) \quad (1)$$

$$(g'_{\rm NGV\,S} - i'_{\rm NGV\,S}) = (g_{\rm ACS} - z_{\rm ACS} + (0.27 \pm 0.02))/(1.65 \pm 0.02) \quad (2)$$

where $g'_{\rm NGV\,S}$, $i'_{\rm NGV\,S}$, $g_{\rm ACS}$, and $z_{\rm ACS}$ represent magnitudes of CFHT g', CFHT i', HST/ACS $F475W$, and HST/ACS $F850LP$, respectively.

For the ACSVCS sources, we define GCs with $p_{GC} \geqslant 0.5$, and $g'_{\rm NGV\,S} \leqslant 24.5$ mag, where p_{GC} is the probability that the object is a GC. We matched these GC candidates to those from the NGVS catalog, and those without a match are added to the total GC samples for further analysis.

2.7. Completeness Test

To estimate the limit of our ground-based photometry, we performed completeness tests by injecting artificial stars into the $10' \times 10'$ cutout images. Artificial stars were constructed using PSFs empirically obtained for each observing field. PSFs were generated with DAOphot, and PSF stars were selected using SExtractor, with inverse concentration indices applied for point-source selection. Detailed information on PSF generation for the NGVS is available on the NGVS webpage, and the process for generating PSFs for MATLAS data closely follows that of the NGVS. When adding these artificial stars, we used a power-law luminosity function with a magnitude range of $20 < g' < 25$. Our GC survey is limited to $g'_0 = 24.5$, so we set the faint magnitude limit to $g' = 25$. When performing these tests, the number of added artificial stars did not exceed 10% of the number of sources with the same magnitude range. We repeated this experiment over 1000 times, resulting in more than 150,000 artificial stars. On average, we added about 200,000 artificial stars to each target image. As expected, the completeness varied with both the magnitude of sources and the background brightness, which generally varies radially from the center of galaxies for ETGs. To account for this variation, we divided the artificial star test into subgroups based on the radial distance from the galaxy center and fitted the

results with a step function as follows:

$$f(m|m_{50}, \alpha) = \frac{1}{2} \times \left(1 - \frac{\alpha(m - m_{50})}{\sqrt{1 + \alpha^2(m - m_{50})^2}}\right) \quad (3)$$

where α is the slope of the decreasing recovery rate; m_{50} is the magnitude for the 50% recovery rate; and m is the magnitude of sources. By applying this method, we obtained the recovery rates that vary with source magnitudes and distances from the galaxy center.

We found that the ground-based photometry suffers from incompleteness near the center of galaxies for the sources with $g' \sim 24.5$ mag, whereas the ACSVCS catalog is 100% complete for the sources with $g_0' \leqslant 24.5$ mag in the entire fields.

2.8. GC Density Profile Fitting

We used an analytic function to investigate the spatial distributions of GCs, especially the GC number density profiles. We fitted these profiles using a two-dimensional Sérsic function plus a constant background, given by

$$\Sigma(R) = \Sigma_e \exp\left\{-b_n\left[\left(\frac{R}{R_e}\right)^{1/n} - 1\right]\right\} + \Sigma_b \quad (4)$$

where

$$R = \sqrt{(X'^2 + Y'^2)/(1 - \epsilon^2)} \quad (5)$$

$$X' = (X - X_0)\cos\theta + (Y - Y_0)\sin\theta \quad (6)$$

$$Y' = (Y - Y_0)\cos\theta - (X - X_0)\sin\theta. \quad (7)$$

Here, θ is the position angle of the GC candidate, measured from north to east, while X_0 and Y_0 are the coordinates of the center of the host galaxy. X and Y are the coordinates of the GC candidates, and ϵ is the ellipticity. In the Sérsic function, R_e is the effective radius, Σ_e is the GC number density at the effective radius, Σ_b is the background GC number density, n is the Sérsic index, and b_n is a constant that depends on n. We used an approximation of b_n (L. Ciotti & G. Bertin 1999).

We fitted this function to the data using a Markov Chain Monte Carlo (MCMC) method with the ∈mcee code in Python (D. Foreman-Mackey et al. 2013). We set flat prior distributions on several parameters, including $\Sigma_e > 0.001$ arcmin^{-2}, $0.25 < n < 8.0$, and $0\farcm05 < R_e < 30'$. Due to difficulties in constraining both ellipticity and position angle in the presence of GC contamination, we imposed priors of $0 \leqslant \epsilon < 0.1$ and $-10^\circ < \theta < 10^\circ$ for most cases. For a handful of elongated galaxies, we also imposed priors of $0 \leqslant \epsilon < 0.4$ and $-180^\circ < \theta < 180^\circ$. We adopted a prior from a Gaussian function with pre-estimated values of the background mean and background standard deviation for the background level.

To obtain the logarithmic probability, we used the following likelihood function:

$$\mathcal{L}(\Sigma_e, n, R_e, \Sigma_b) \propto \prod_i \ell_i(R_i|\Sigma_e, n, R_e, \Sigma_b). \quad (8)$$

Here, $\ell_i(R_i|\Sigma_e, n, R_e, \Sigma_n)$ is the probability of finding datum i at radius R_i given the Sérsic parameters. We applied a completeness correction to each data point R_i for galaxies without HST data. This completeness correction involved convolving the source detection probability function for CFHT/MegaCam data with the intrinsic luminosity function, which allowed the density probability function to be corrected for each data point.

To construct the probability function, we need to integrate the modified Sérsic function. As our modified Sérsic function does not have a theoretical integrated function form, we used a numerical integration method to generate the probability function. The integration range is normally from the radius corresponding to the 50% completeness limit to $30'$. If ACSVCS imaging is available, the integration starts at the galaxy center. For the largest galaxies, the outer limit was taken to be $60'$.

We also masked unfavorable areas for GC density profile fitting: i.e., those regions affected by saturated stars, nearby galaxies, or outside of the observation fields, etc. In the case of target galaxies with neighbors, we fit two two-dimensional Sérsic functions, simultaneously, to include the contribution from the neighboring galaxy. However, if there are more than two neighboring target galaxies, then we masked them except for the most dominant neighbor.

2.9. Color Distribution of GCs

The colors of GCs in ETGs are often used as a metallicity indicator, and they typically show unimodal or bimodal distributions. We used Gaussian mixture modeling (GMM; A. L. Muratov & O. Y. Gnedin 2010) to test for color-bimodality among the GC systems. To create input catalogs for the GMM test, we selected GCs within a radius of $2.5R_{e,gc}$, and used their $(g - i)$ colors. However, these GCs can be contaminated by various sources, including intracluster GCs, foreground stars, and background galaxies. To deal with background contamination, we followed several steps: (1) We defined a background area outside the galaxy region and calculated the areal fraction between the background field and the galaxy field (within $2.5R_{e,gc}$); we then randomly chose background objects based on this areal fraction; (2) we subtracted GCs in the galaxy region that had the closest colors to the GC candidates in the background region; (3) using this background-subtracted catalog, we ran the GMM code and obtained the results; (4) we repeated this process 30 times to account for errors in background subtraction. After these steps, we calculated the mean and standard deviation of D-values, representing the distances between the peaks of the fitted Gaussian functions. If the D-value was greater than 2, it indicates the data were better fit by two Gaussian functions, and we considered the distribution bimodal when the D-values were greater than two standard deviations. For GCs with a D-value greater than 2, we divided them into blue and red GCs based on the crossover values of the two fitted Gaussian functions.

2.10. Total Number of GCs

The total number of GCs is a fundamental parameter in the study of GC systems. However, estimating this number requires overcoming the observational limits of magnitudes and spatial coverage. In this study, we used the two-dimensional Sérsic fitting of the GC distribution to estimate the total number of GCs above the magnitude limit ($g_0' = 24.5$ mag). We integrated the fitted two-dimensional Sérsic function to obtain the magnitude-limited total number of GCs.

It is well known that GC luminosity functions (GCLFs) have a roughly universal Gaussian form with a peak luminosity of $M_V \sim -7.5$ (e.g., W. E. Harris 2001; M. G. Lee 2003). More

precisely, peaks and widths of GCLFs change slightly depending on the host galaxy luminosity (e.g., A. Jordán et al. 2007b; D. Villegas et al. 2010). We made a similar assumption by adopting different peak luminosities and widths of the Gaussian function based on the host galaxy luminosity, using the relation from D. Villegas et al. (2010). D. Villegas et al. (2010) also provides mean and σ values for the GCLF of many target galaxies in this study, so we used these values directly for these common targets. With these GCLFs, we could correct the observation's magnitude limit and obtain the total number of GCs. We were also able to estimate the errors of the GC total numbers based on the errors of the Sérsic fitting, but we did not include the errors from GCLF. Note that the total number of GCs for ACSVCS galaxies has been calculated based on the HST data (E. W. Peng et al. 2008); we will compare both numbers and discuss them in the next section.

3. Results and Discussions

3.1. GC Properties

Table 2 presents the estimated properties of the GC systems in our target galaxies. The table provides information on the effective radii and total numbers of GC systems with their 1σ errors. Additionally, we include the Sérsic indices, n, for all GC systems. The table also notes the bimodality of GC colors, indicating the effective radii and peak colors of the blue and red GCs for those galaxies that exhibit a bimodal GC color distribution. The table also includes the median GC colors for those galaxies exhibiting an unimodal GC color distribution. Furthermore, the GC specific frequency is also noted (see the bottom of this section).

The effective radii of GC systems ($R_{e,gc}$) vary from subarcminutes to approximately 16′. For instance, NGC 4649 has the largest $R_{e,gc}$, and VCC 1539 has the smallest $R_{e,gc}$, on an arcminute scale. Sérsic n values also vary within our fitting range, with most targets having Sérsic n values ranging from approximately 0.5–4. However, many program objects show substantial errors in their measured Sérsic n values due to a small number of GCs. The total number of GCs ranges from less than 10, for the faint dwarfs, to 10,000 or more for the brightest giants. NGC 4486 has the largest number of GCs, while VCC 1993 has the smallest number of GCs.

For each program galaxy, results are shown in a series of four figures. These are as follows: (1) a two-dimensional number density map of GC candidates; a mask map, which we used for Sérsic fitting, is overlaid on the number density map; (2) a two-dimensional and marginalized posterior probability density function; $R_{e,gc}$, Sérsic n, and constant background are shown; (3) a one-dimensional radial GC number density profile with fitted model; in each case, we show the fitted Sérsic function, the best-fit constant background, and their sum; and (4) a $(g - i)$ color distribution of GC candidates within $2.5R_{e,gc}$. We show the two fitted Gaussian functions and their peaks if it is bimodal. If the color distribution is unimodal, then we show a location of median color. These four figures for all the unimodal and bimodal targets are shown in the figures sets of Figures 3 and 4, respectively.

We make notes for individual galaxies in the Appendix, but here, we point out some notable features or peculiarities for our sample galaxies:

1. *Peculiar spatial distributions.* NGC 1023, NGC 4442, and NGC 4608 display elongated spatial distributions of GCs. The GC number density peaks in NGC 2685, VCC 200, IC 3328, VCC 1512, VCC 1833, UGC 7854, VCC 1993, and PGC 058114 are offset from the galaxy centers. NGC 3098, on the other hand, appears to show a lopsided distribution of GCs.
2. *Exceptional color distributions.* NGC 4564 contains a notably large population of red GCs. NGC 4694 also exhibits a large fraction of red GCs, although, in this case, the results might be influenced by the existence of a large population of green GCs. NGC 7454 stands out as having an unimodal GC population containing relatively red GCs.
3. *Sparse GC systems.* NGC 6548 and NGC 7280 contain almost no GCs within $2_{Re,GC}$, which may indicate that our fitting results are unreliable for these galaxies.

We compare our GC number density profile of NGC 4486 with those from the literature to check for consistency (Figure 5). Each study has different magnitude limits in different filter systems, so all data points in Figure 5 are background subtracted and corrected to full GCLF. All three data sets (this study; D. E. McLaughlin 1999; and W. E. Harris 2009) show consistent results. To assess the reliability of using the GCLF parameters from D. Villegas et al. (2010), we also estimated the σ of the GCLFs using our data and compared these values with those reported by D. Villegas et al. (2010; Figure 6). The σ values from our study are consistent with those of D. Villegas et al. (2010), supporting our decision to use their GCLF parameters to estimate the total number of GCs.

We also estimated GC specific frequency of our samples. Traditionally, GC specific frequency is calculated with the V-band absolute magnitude of the host galaxy, but we estimated it with g'-band absolute magnitude of the host galaxy. We calculate GC specific frequency ($S_{N,g'}$) with the following equation:

$$S_{N,g'} = N_{\rm GC} \times 10^{0.4(M_{g'}+15)}. \quad (9)$$

Figure 7 shows relations between host galaxy magnitudes and $S_{N,g'}$. It shows a typical U-shape, and M87 has the highest $S_{N,g'}$ among massive galaxies. We marked MATLAS samples, and they mostly have low $S_{N,g'}$ except for three galaxies (NGC 4278, NGC 4283, and NGC 5846).

3.2. Comparison of the Total Number of GCs with the ACSVCS

Seventy-five targets in this study overlap with those in the ACSVCS, providing the total number of GCs. We compare these total numbers with those from E. W. Peng et al. (2008) in Figure 8. The direct comparison shows that this study's total number of GCs is slightly larger than that in the ACSVCS. The agreement is better for larger numbers, as the ACSVCS includes additional data outside the ACS/Wide Field Channel (WFC) FoV for large galaxies (marked with large open circles in the left panel of Figure 8). While we might expect good agreement for medium and low-number GCs, the differences in total GC numbers between this study and the ACSVCS increase as the total number of GCs decreases.

To investigate this trend, we compare the total number of GCs in the ACSVCS with the results from this study but limit it to GCs within 1.′67 from the galaxy center to match the ACS/WFC FoV, as shown in the right panel of Figure 8. Galaxies with about 100 GCs have consistent results between the ACSVCS and this study, suggesting that the number of GCs in intermediate-luminosity galaxies with $N_{\rm GC,Total} \approx 100$ may be underestimated in the ACSVCS due to the limit of the ACS

Table 2
GC Properties from This Study

Name	$R_{e,gc}$ (arcmin)	Sérsic n	$N_{\rm GC}$	Bimodality	$R_{e,\rm bgc}$ (arcmin)	$R_{e,rgc}$ (arcmin)	$(g-i)_{0,b}$	$(g-i)_{0,r}$	$(g-i)_{0,m}$	$S_{N,g'}$
(1)	(2)	(3)	(4)	(5)	(6)	(7)	(8)	(9)	(10)	(11)
NGC 0524	$2.69^{+0.39}_{-0.24}$	$2.58^{+0.90}_{-0.56}$	1459^{+277}_{-211}	N	...	...	...	...	0.86	$6.9^{+1.3}_{-1.0}$
NGC 0821	$1.17^{+0.43}_{-0.28}$	$5.38^{+1.73}_{-1.90}$	764^{+315}_{-230}	Y	$1.51^{+0.70}_{-0.43}$	$0.53^{+0.27}_{-0.15}$	0.76	1.01	...	$4.3^{+1.8}_{-1.3}$
NGC 0936	$2.22^{+1.24}_{-0.68}$	$6.71^{+0.93}_{-1.40}$	1265^{+452}_{-413}	Y	$4.47^{+2.80}_{-1.55}$	$1.12^{+0.52}_{-0.43}$	0.74	1.00	...	$4.3^{+1.6}_{-1.4}$
NGC 1023	$1.72^{+0.60}_{-0.43}$	$4.12^{+2.34}_{-2.28}$	304^{+104}_{-93}	Y	$2.05^{+1.23}_{-0.75}$	$1.55^{+0.32}_{-0.44}$	0.67	0.92	...	$2.5^{+0.9}_{-0.8}$
NGC 2592	$0.73^{+0.31}_{-0.20}$	$4.90^{+2.07}_{-1.96}$	269^{+72}_{-67}	N	...	...	...	...	0.81	$6.3^{+1.7}_{-1.6}$
NGC 2685	$1.65^{+0.78}_{-0.75}$	$2.85^{+3.57}_{-2.12}$	50^{+28}_{-19}	Y	$1.35^{+0.83}_{-0.69}$	$0.61^{+0.87}_{-0.33}$	0.80	1.10	...	$1.1^{+0.6}_{-0.4}$
NGC 2768	$1.45^{+0.46}_{-0.37}$	$5.58^{+1.59}_{-1.86}$	1012^{+307}_{-225}	Y	$1.78^{+0.54}_{-0.37}$	$0.46^{+0.24}_{-0.13}$	0.73	0.98	...	$4.4^{+1.3}_{-1.0}$
NGC 2778	$1.54^{+0.88}_{-0.69}$	$5.20^{+2.04}_{-2.29}$	94^{+50}_{-36}	Y	$2.92^{+1.84}_{-1.34}$	$0.26^{+0.23}_{-0.13}$	0.77	1.14	...	$3.0^{+1.6}_{-1.1}$
NGC 2950	$0.67^{+0.34}_{-0.20}$	$3.21^{+3.11}_{-1.83}$	83^{+31}_{-26}	Y	$0.86^{+0.59}_{-0.31}$	$0.58^{+0.36}_{-0.24}$	0.66	0.91	...	$1.4^{+0.5}_{-0.4}$
NGC 3098	$1.51^{+1.11}_{-0.58}$	$4.72^{+2.22}_{-2.45}$	123^{+60}_{-39}	N	...	...	...	...	0.79	$2.5^{+1.2}_{-0.8}$
NGC 3245	$0.85^{+0.37}_{-0.24}$	$5.10^{+1.77}_{-1.94}$	325^{+88}_{-82}	Y	$1.23^{+0.40}_{-0.32}$	$0.36^{+0.20}_{-0.11}$	0.74	1.04	...	$3.0^{+0.8}_{-0.8}$
NGC 3379	$1.97^{+0.06}_{-0.07}$	$7.97^{+0.02}_{-0.05}$	352^{+22}_{-26}	Y	$2.02^{+0.06}_{-0.03}$	$0.84^{+0.06}_{-0.06}$	0.77	1.03	...	$3.3^{+0.2}_{-0.2}$
NGC 3384	$0.93^{+0.10}_{-0.10}$	$0.52^{+0.17}_{-0.16}$	50^{+10}_{-9}	Y	$1.09^{+0.03}_{-0.06}$	$1.08^{+0.05}_{-0.05}$	0.77	0.97	...	$0.6^{+0.1}_{-0.1}$
NGC 3457	$0.34^{+0.13}_{-0.07}$	$1.56^{+3.45}_{-1.01}$	39^{+18}_{-13}	N	...	...	...	...	0.85	$1.5^{+0.7}_{-0.5}$
NGC 3489	$1.07^{+0.68}_{-0.37}$	$4.84^{+2.23}_{-2.46}$	114^{+35}_{-36}	Y	$0.83^{+0.51}_{-0.29}$	$0.86^{+1.10}_{-0.49}$	0.73	1.19	...	$1.6^{+0.5}_{-0.5}$
NGC 3599	$0.83^{+0.44}_{-0.31}$	$3.69^{+2.83}_{-2.15}$	97^{+35}_{-27}	N	...	...	...	...	0.80	$2.4^{+0.9}_{-0.7}$
NGC 3607	$2.03^{+0.09}_{-0.07}$	$7.97^{+0.03}_{-0.07}$	865^{+77}_{-61}	Y	$1.70^{+0.06}_{-0.04}$	$1.70^{+0.08}_{-0.07}$	0.81	1.05	...	$2.9^{+0.3}_{-0.2}$
NGC 3608	$2.01^{+0.13}_{-0.11}$	$1.56^{+0.30}_{-0.21}$	376^{+60}_{-37}	Y	$1.14^{+0.15}_{-0.12}$	$0.96^{+0.06}_{-0.08}$	0.76	1.03	...	$3.8^{+0.6}_{-0.4}$
NGC 3630	$1.82^{+2.09}_{-0.85}$	$6.83^{+0.83}_{-1.93}$	305^{+227}_{-118}	N	...	...	...	...	0.73	$4.6^{+3.4}_{-1.8}$
NGC 3945	$1.75^{+1.06}_{-0.52}$	$2.67^{+3.02}_{-1.98}$	119^{+66}_{-47}	Y	$2.07^{+1.07}_{-0.74}$	$0.95^{+0.63}_{-0.40}$	0.70	1.07	...	$0.6^{+0.3}_{-0.2}$
IC 3032	$0.45^{+0.27}_{-0.19}$	$2.06^{+2.36}_{-1.24}$	9^{+6}_{-4}	N	...	...	...	...	0.86	$3.8^{+2.6}_{-1.7}$
IC 3065	$0.70^{+0.50}_{-0.32}$	$2.81^{+2.18}_{-1.28}$	45^{+17}_{-14}	N	...	...	...	...	0.76	$6.4^{+2.4}_{-2.0}$
VCC 200	$0.28^{+0.08}_{-0.07}$	$0.80^{+1.28}_{-1.28}$	24^{+10}_{-8}	N	...	...	...	...	0.68	$5.1^{+2.1}_{-1.6}$
IC 3101	$0.29^{+0.07}_{-0.05}$	$3.13^{+0.91}_{-1.33}$	31^{+14}_{-10}	N	...	...	...	...	0.71	$13.4^{+6.1}_{-4.3}$
NGC 4262	$1.69^{+0.65}_{-0.49}$	$2.58^{+0.99}_{-0.87}$	154^{+46}_{-38}	Y	$2.76^{+1.40}_{-0.93}$	$0.58^{+0.30}_{-0.19}$	0.70	1.07	...	$3.9^{+1.2}_{-1.0}$
NGC 4267	$0.97^{+0.05}_{-0.05}$	$0.46^{+0.12}_{-0.08}$	229^{+42}_{-38}	Y	$0.97^{+0.21}_{-0.14}$	$0.97^{+0.06}_{-0.06}$	0.75	0.95	...	$3.1^{+0.6}_{-0.5}$
NGC 4278	$2.53^{+0.11}_{-0.08}$	$3.12^{+0.16}_{-0.09}$	1188^{+98}_{-73}	Y	$1.22^{+0.03}_{-0.08}$	$1.15^{+0.06}_{-0.07}$	0.79	1.02	...	$10.3^{+0.8}_{-0.6}$
NGC 4283	$1.00^{+0.12}_{-0.10}$	$7.99^{+0.01}_{-0.02}$	192^{+54}_{-38}	Y	$3.01^{+0.06}_{-0.04}$	$0.21^{+0.03}_{-0.01}$	0.71	1.02	...	$10.0^{+2.8}_{-2.0}$
UGC 7436	$0.42^{+0.23}_{-0.16}$	$5.84^{+1.50}_{-1.97}$	38^{+15}_{-12}	N	...	...	...	...	0.72	$6.1^{+2.3}_{-1.8}$
VCC 571	$0.12^{+0.12}_{-0.05}$	$5.16^{+1.99}_{-2.70}$	19^{+9}_{-7}	N	...	...	...	...	0.75	$3.0^{+1.4}_{-1.2}$
NGC 4318	$0.47^{+0.35}_{-0.19}$	$6.68^{+0.97}_{-2.21}$	43^{+28}_{-19}	Y	$0.22^{+0.32}_{-0.10}$	$0.46^{+0.40}_{-0.22}$	0.66	0.89	...	$2.6^{+1.7}_{-1.1}$
NGC 4339	$1.34^{+0.17}_{-0.13}$	$1.05^{+0.25}_{-0.25}$	223^{+30}_{-26}	N	...	...	...	...	0.83	$4.7^{+0.6}_{-0.6}$
NGC 4340	$0.76^{+0.08}_{-0.10}$	$0.86^{+0.12}_{-0.16}$	76^{+19}_{-23}	Y	$0.83^{+0.10}_{-0.10}$	$0.77^{+0.08}_{-0.07}$	0.67	0.94	...	$1.0^{+0.2}_{-0.3}$
NGC 4342	$1.76^{+2.84}_{-0.10}$	$0.73^{+4.72}_{-0.12}$	527^{+54}_{-107}	Y	$1.11^{+0.09}_{-0.06}$	$1.07^{+0.05}_{-0.07}$	0.69	0.82	...	$20.6^{+2.1}_{-4.2}$
NGC 4350	$2.31^{+0.16}_{-0.22}$	$2.99^{+0.12}_{-0.13}$	459^{+73}_{-80}	Y	$2.41^{+0.16}_{-0.24}$	$1.36^{+0.93}_{-0.53}$	0.73	0.98	...	$6.1^{+1.0}_{-1.1}$
NGC 4352	$0.59^{+0.05}_{-0.04}$	$0.86^{+0.30}_{-0.20}$	158^{+41}_{-39}	N	...	...	...	...	0.74	$6.8^{+1.7}_{-1.7}$
NGC 4365	$3.73^{+0.13}_{-0.11}$	$2.04^{+0.17}_{-0.11}$	3887^{+243}_{-238}	Y	$4.95^{+0.31}_{-0.29}$	$2.92^{+0.16}_{-0.14}$	0.72	0.95	...	$6.1^{+0.4}_{-0.4}$
NGC 4371	$1.03^{+0.27}_{-0.18}$	$2.58^{+0.92}_{-0.63}$	277^{+81}_{-59}	Y	$1.42^{+0.95}_{-0.47}$	$0.98^{+0.28}_{-0.15}$	0.74	1.01	...	$2.8^{+0.8}_{-0.6}$
NGC 4374	$6.18^{+4.74}_{-0.60}$	$2.71^{+0.31}_{-0.24}$	3080^{+388}_{-319}	Y	$7.93^{+0.82}_{-0.72}$	$3.17^{+0.36}_{-0.26}$	0.73	0.99	...	$4.7^{+0.6}_{-0.5}$
NGC 4377	$0.42^{+0.08}_{-0.05}$	$0.87^{+0.50}_{-0.40}$	83^{+24}_{-19}	Y	$0.58^{+0.20}_{-0.12}$	$0.34^{+0.07}_{-0.05}$	0.73	0.97	...	$2.0^{+0.6}_{-0.5}$
NGC 4379	$0.52^{+0.16}_{-0.09}$	$1.78^{+1.33}_{-0.60}$	92^{+27}_{-18}	N	...	...	...	...	0.86	$2.5^{+0.7}_{-0.5}$
NGC 4387	$0.68^{+0.31}_{-0.19}$	$1.66^{+1.00}_{-0.72}$	62^{+39}_{-24}	Y	$0.98^{+0.35}_{-0.36}$	$0.35^{+0.20}_{-0.11}$	0.69	0.91	...	$2.0^{+1.3}_{-0.8}$
IC 3328	$0.50^{+0.13}_{-0.10}$	$2.84^{+1.35}_{-0.93}$	68^{+21}_{-15}	N	...	...	...	...	0.77	$8.9^{+2.7}_{-2.0}$
NGC 4406	$7.16^{+0.69}_{-0.52}$	$1.95^{+0.19}_{-0.14}$	3261^{+394}_{-315}	Y	$8.35^{+0.96}_{-0.82}$	$4.58^{+0.47}_{-0.36}$	0.71	0.97	...	$4.2^{+0.5}_{-0.4}$
NGC 4417	$0.93^{+0.08}_{-0.10}$	$1.98^{+0.18}_{-0.18}$	100^{+17}_{-23}	Y	$1.04^{+0.18}_{-0.16}$	$0.48^{+0.06}_{-0.06}$	0.72	0.99	...	$1.6^{+0.3}_{-0.4}$
NGC 4425	$1.71^{+0.18}_{-0.16}$	$7.85^{+0.09}_{-0.10}$	213^{+58}_{-42}	Y	$0.60^{+0.04}_{-0.04}$	$0.37^{+0.05}_{-0.06}$	0.69	0.87	...	$6.6^{+1.8}_{-1.3}$
NGC 4429	$1.01^{+0.28}_{-0.16}$	$1.94^{+2.72}_{-1.07}$	269^{+179}_{-92}	Y	$0.70^{+0.36}_{-0.26}$	$1.20^{+0.46}_{-0.23}$	0.70	0.97	...	$1.4^{+0.9}_{-0.5}$
NGC 4434	$0.95^{+0.21}_{-0.14}$	$4.35^{+1.46}_{-1.46}$	159^{+27}_{-23}	N	...	...	...	...	0.74	$3.0^{+0.5}_{-0.4}$
NGC 4435	$0.90^{+0.09}_{-0.09}$	$1.74^{+0.36}_{-0.32}$	224^{+34}_{-28}	Y	$1.17^{+0.20}_{-0.22}$	$0.77^{+0.09}_{-0.07}$	0.73	0.99	...	$2.0^{+0.3}_{-0.2}$
NGC 4442	$1.09^{+0.11}_{-0.09}$	$1.24^{+0.30}_{-0.21}$	308^{+38}_{-34}	Y	$1.35^{+0.22}_{-0.16}$	$0.85^{+0.10}_{-0.09}$	0.74	1.00	...	$3.0^{+0.4}_{-0.3}$
IC 3383	$0.54^{+0.19}_{-0.11}$	$7.92^{+0.07}_{-0.19}$	29^{+14}_{-11}	N	...	...	...	...	0.72	$7.8^{+3.7}_{-2.9}$
IC 3381	$1.04^{+0.37}_{-0.23}$	$6.28^{+1.20}_{-1.63}$	125^{+44}_{-35}	N	...	...	...	...	0.72	$7.5^{+2.6}_{-2.1}$
NGC 4452	$2.09^{+1.13}_{-0.85}$	$5.08^{+1.62}_{-1.58}$	155^{+71}_{-53}	Y	$1.51^{+0.83}_{-0.52}$	$0.23^{+0.33}_{-0.11}$	0.70	1.06	...	$6.6^{+3.0}_{-2.2}$
NGC 4458	$0.61^{+0.15}_{-0.10}$	$2.14^{+1.16}_{-0.68}$	124^{+34}_{-30}	N	...	...	...	...	0.93	$3.9^{+1.1}_{-0.9}$
NGC 4459	$1.10^{+0.14}_{-0.10}$	$1.35^{+0.32}_{-0.27}$	278^{+38}_{-31}	Y	$1.45^{+0.47}_{-0.28}$	$0.88^{+0.11}_{-0.09}$	0.78	1.00	...	$1.8^{+0.2}_{-0.2}$
NGC 4461	$2.12^{+0.23}_{-0.19}$	$1.92^{+0.19}_{-0.23}$	288^{+62}_{-48}	Y	$0.67^{+0.04}_{-0.04}$	$0.67^{+0.06}_{-0.07}$	0.68	1.02	...	$4.2^{+0.9}_{-0.7}$
VCC 1185	$0.59^{+0.12}_{-0.17}$	$1.38^{+0.48}_{-0.32}$	30^{+14}_{-12}	N	...	...	...	...	0.71	$11.6^{+5.4}_{-4.6}$
NGC 4472	$10.66^{+0.54}_{-0.43}$	$2.45^{+0.12}_{-0.13}$	9826^{+839}_{-758}	Y	$13.95^{+0.45}_{-0.45}$	$5.34^{+0.25}_{-0.23}$	0.72	1.01	...	$8.6^{+0.7}_{-0.7}$
NGC 4473	$2.48^{+0.88}_{-0.45}$	$3.14^{+0.81}_{-0.56}$	674^{+161}_{-132}	Y	$4.11^{+1.82}_{-1.11}$	$1.40^{+0.27}_{-0.18}$	0.73	0.98	...	$4.6^{+1.1}_{-0.9}$
NGC 4474	$0.93^{+0.24}_{-0.15}$	$2.69^{+1.01}_{-0.67}$	183^{+39}_{-28}	N	...	...	...	...	0.84	$4.5^{+1.0}_{-0.7}$
NGC 4476	$0.49^{+0.14}_{-0.13}$	$2.98^{+0.83}_{-0.83}$	30^{+14}_{-10}	N	...	...	...	...	0.77	$0.9^{+0.4}_{-0.3}$
NGC 4477	$1.98^{+0.10}_{-0.11}$	$1.50^{+0.15}_{-0.16}$	264^{+22}_{-29}	Y	$2.01^{+0.10}_{-0.05}$	$1.97^{+0.05}_{-0.05}$	0.74	1.07	...	$2.1^{+0.2}_{-0.2}$
NGC 4482	$0.98^{+0.60}_{-0.40}$	$3.95^{+2.20}_{-1.51}$	79^{+39}_{-30}	N	...	...	...	...	0.76	$4.5^{+2.2}_{-1.8}$
NGC 4478	$0.59^{+0.10}_{-0.07}$	$2.63^{+0.89}_{-0.89}$	145^{+58}_{-30}	Y	$0.71^{+0.13}_{-0.09}$	$0.60^{+0.16}_{-0.13}$	0.70	0.94	...	$2.5^{+1.0}_{-0.5}$
NGC 4479	$0.77^{+0.13}_{-0.15}$	$2.99^{+0.80}_{-0.80}$	49^{+18}_{-13}	Y	$0.47^{+0.06}_{-0.06}$	$0.29^{+0.07}_{-0.05}$	0.72	1.04	...	$2.5^{+0.9}_{-0.7}$

Table 2
(Continued)

Name	$R_{e,gc}$ (arcmin)	Sérsic n	N_{GC}	Bimodality	$R_{e,bgc}$ (arcmin)	$R_{e,rgc}$ (arcmin)	$(g-i)_{0,b}$	$(g-i)_{0,r}$	$(g-i)_{0,m}$	$S_{N,g'}$
(1)	(2)	(3)	(4)	(5)	(6)	(7)	(8)	(9)	(10)	(11)
NGC 4483	$1.19^{+0.62}_{-0.42}$	$4.64^{+1.87}_{-1.47}$	103^{+27}_{-24}	Y	$1.06^{+0.49}_{-0.33}$	$0.08^{+0.07}_{-0.02}$	0.67	0.90	...	$4.2^{+1.1}_{-1.0}$
NGC 4486	$13.67^{+0.88}_{-0.77}$	$3.76^{+0.14}_{-0.17}$	$17,730^{+1030}_{-942}$	Y	$15.22^{+1.22}_{-1.30}$	$4.00^{+0.23}_{-0.20}$	0.70	0.99	...	$22.6^{+1.3}_{-1.2}$
NGC 4489	$0.53^{+0.31}_{-0.11}$	$2.04^{+2.32}_{-0.90}$	72^{+25}_{-19}	N	...	...	...	...	0.75	$3.2^{+1.1}_{-0.8}$
IC 3461	$0.16^{+0.02}_{-0.02}$	$1.40^{+0.24}_{-0.20}$	35^{+12}_{-9}	Y	$0.38^{+0.08}_{-0.07}$	$0.23^{+0.05}_{-0.05}$	0.71	0.90	...	$10.1^{+3.4}_{-2.7}$
NGC 4503	$2.01^{+0.09}_{-0.12}$	$3.04^{+0.23}_{-0.33}$	376^{+44}_{-54}	Y	$1.97^{+0.44}_{-0.33}$	$0.58^{+0.05}_{-0.05}$	0.72	1.03	...	$5.5^{+0.7}_{-0.8}$
IC 3468	$0.27^{+0.15}_{-0.08}$	$4.44^{+2.29}_{-2.01}$	39^{+12}_{-10}	Y	$0.36^{+0.35}_{-0.15}$	$0.25^{+0.20}_{-0.08}$	0.74	0.89	...	$3.0^{+0.9}_{-0.8}$
IC 3470	$0.37^{+0.07}_{-0.06}$	$1.55^{+0.82}_{-0.45}$	87^{+18}_{-16}	Y	$0.36^{+0.04}_{-0.03}$	$0.42^{+0.28}_{-0.18}$	0.76	0.99	...	$15.1^{+3.1}_{-2.7}$
IC 798	$0.45^{+0.11}_{-0.09}$	$7.89^{+0.10}_{-0.34}$	61^{+22}_{-22}	N	...	...	...	...	0.69	$14.6^{+5.3}_{-5.4}$
NGC 4515	$0.56^{+0.27}_{-0.11}$	$2.23^{+1.67}_{-0.82}$	115^{+38}_{-23}	N	...	...	...	...	0.73	$6.2^{+2.1}_{-1.2}$
VCC 1512	$0.31^{+0.40}_{-0.14}$	$3.99^{+2.75}_{-2.75}$	14^{+10}_{-6}	N	...	...	...	...	0.64	$5.7^{+4.4}_{-2.6}$
IC 3501	$0.56^{+0.20}_{-0.12}$	$2.40^{+1.30}_{-0.81}$	63^{+17}_{-14}	N	...	...	...	...	0.77	$11.8^{+3.3}_{-2.7}$
NGC 4528	$1.55^{+1.40}_{-0.60}$	$2.44^{+1.43}_{-1.01}$	83^{+41}_{-27}	N	...	...	...	...	2.18	$3.1^{+1.5}_{-1.0}$
VCC 1539	$0.15^{+0.03}_{-0.03}$	$1.24^{+2.19}_{-0.63}$	45^{+13}_{-11}	N	...	...	...	...	0.76	$29.2^{+8.4}_{-6.9}$
IC 3509	$0.47^{+0.07}_{-0.06}$	$2.46^{+0.45}_{-0.57}$	71^{+20}_{-14}	Y	$0.44^{+0.12}_{-0.09}$	$0.42^{+0.17}_{-0.13}$	0.61	0.81	...	$20.9^{+5.8}_{-4.0}$
NGC 4550	$0.77^{+0.05}_{-0.05}$	$2.32^{+0.07}_{-0.06}$	97^{+14}_{-10}	Y	$0.62^{+0.03}_{-0.02}$	$0.49^{+0.03}_{-0.04}$	0.67	0.92	...	$2.7^{+0.4}_{-0.3}$
NGC 4551	$0.62^{+0.08}_{-0.08}$	$3.70^{+0.07}_{-0.07}$	68^{+19}_{-15}	Y	$0.54^{+0.08}_{-0.06}$	$0.28^{+0.05}_{-0.05}$	0.72	1.01	...	$2.3^{+0.6}_{-0.5}$
NGC 4552	$4.26^{+0.57}_{-0.46}$	$3.36^{+0.38}_{-0.33}$	1822^{+174}_{-143}	Y	$6.35^{+1.52}_{-1.16}$	$2.39^{+0.38}_{-0.26}$	0.72	0.99	...	$6.8^{+0.7}_{-0.5}$
VCC 1661	$0.27^{+0.06}_{-0.05}$	$7.87^{+0.10}_{-0.33}$	26^{+12}_{-9}	N	...	...	...	...	0.72	$18.2^{+8.1}_{-6.5}$
NGC 4564	$0.76^{+0.14}_{-0.08}$	$2.10^{+0.61}_{-0.45}$	218^{+69}_{-63}	Y	$1.11^{+0.65}_{-0.38}$	$0.68^{+0.09}_{-0.07}$	0.69	0.94	...	$3.3^{+1.0}_{-1.0}$
NGC 4570	$1.33^{+0.24}_{-0.19}$	$2.37^{+0.69}_{-0.46}$	261^{+70}_{-73}	Y	$1.76^{+0.61}_{-0.35}$	$0.57^{+0.10}_{-0.08}$	0.70	1.01	...	$2.7^{+0.7}_{-0.8}$
NGC 4578	$1.15^{+1.09}_{-0.36}$	$2.53^{+1.67}_{-1.38}$	90^{+49}_{-29}	Y	$1.49^{+0.59}_{-0.61}$	$0.66^{+0.19}_{-0.12}$	0.70	1.06	...	$1.8^{+1.0}_{-0.6}$
NGC 4596	$2.14^{+0.98}_{-0.62}$	$6.45^{+1.10}_{-1.70}$	1010^{+212}_{-210}	Y	$2.83^{+1.30}_{-0.85}$	$1.10^{+0.63}_{-0.38}$	0.73	0.99	...	$6.6^{+1.4}_{-1.4}$
VCC 1826	$0.79^{+0.62}_{-0.36}$	$2.06^{+2.06}_{-1.23}$	14^{+11}_{-8}	N	...	...	...	...	0.72	$8.1^{+6.3}_{-4.4}$
VCC 1833	$0.34^{+0.19}_{-0.12}$	$3.52^{+2.86}_{-1.87}$	28^{+12}_{-9}	N	...	...	...	...	0.74	$5.6^{+2.4}_{-1.8}$
IC 3647	$0.34^{+0.05}_{-0.05}$	$0.63^{+0.85}_{-0.30}$	18^{+7}_{-4}	Y	$0.33^{+0.05}_{-0.04}$	$0.42^{+0.35}_{-0.19}$	0.70	0.94	...	$3.1^{+1.1}_{-0.8}$
IC 3652	$0.77^{+0.13}_{-0.12}$	$1.89^{+0.63}_{-0.63}$	60^{+20}_{-15}	Y	$0.92^{+0.14}_{-0.14}$	$0.43^{+0.11}_{-0.10}$	0.69	0.99	...	$8.0^{+2.6}_{-2.1}$
NGC 4608	$3.45^{+0.93}_{-0.89}$	$3.62^{+2.84}_{-1.97}$	287^{+130}_{-94}	Y	$3.40^{+1.01}_{-1.09}$	$0.38^{+0.48}_{-0.24}$	0.71	1.08	...	$3.8^{+1.7}_{-1.2}$
IC 3653	$0.41^{+0.11}_{-0.10}$	$2.12^{+0.31}_{-0.31}$	14^{+9}_{-6}	N	...	...	...	...	0.71	$2.3^{+1.4}_{-1.0}$
NGC 4612	$0.88^{+0.23}_{-0.17}$	$2.34^{+0.85}_{-0.60}$	159^{+50}_{-41}	N	...	...	...	...	0.81	$2.5^{+0.8}_{-0.7}$
VCC 1886	$0.25^{+0.10}_{-0.06}$	$1.17^{+0.49}_{-0.49}$	7^{+6}_{-3}	N	...	...	...	...	0.77	$3.0^{+2.7}_{-1.3}$
UGC 7854	$0.97^{+0.22}_{-0.17}$	$0.50^{+0.42}_{-0.20}$	18^{+10}_{-6}	N	...	...	...	...	0.75	$5.7^{+3.0}_{-1.8}$
NGC 4621	$4.48^{+0.72}_{-0.56}$	$3.26^{+0.33}_{-0.31}$	1318^{+132}_{-110}	Y	$5.90^{+0.88}_{-0.83}$	$3.29^{+0.41}_{-0.39}$	0.73	0.98	...	$5.2^{+0.5}_{-0.4}$
NGC 4638	$1.62^{+0.35}_{-0.22}$	$1.31^{+0.52}_{-0.52}$	234^{+62}_{-51}	N	...	...	...	...	0.74	$3.3^{+0.9}_{-0.7}$
NGC 4649	$15.71^{+0.41}_{-0.38}$	$4.57^{+0.16}_{-0.16}$	8875^{+508}_{-419}	Y	$13.88^{+1.09}_{-1.05}$	$3.47^{+0.18}_{-0.17}$	0.70	0.99	...	$14.2^{+0.8}_{-0.7}$
VCC 1993	$0.65^{+0.47}_{-0.24}$	$1.10^{+1.02}_{-0.63}$	6^{+7}_{-3}	N	...	...	...	...	0.67	$2.6^{+2.9}_{-1.4}$
NGC 4660	$1.06^{+0.24}_{-0.14}$	$2.54^{+0.66}_{-0.48}$	291^{+50}_{-36}	N	...	...	...	...	0.76	$5.5^{+0.9}_{-0.7}$
IC 3735	$0.45^{+0.34}_{-0.17}$	$4.18^{+2.45}_{-1.92}$	28^{+14}_{-10}	N	...	...	...	...	0.76	$4.5^{+2.3}_{-1.6}$
IC 3773	$0.32^{+0.20}_{-0.11}$	$3.73^{+2.69}_{-2.22}$	19^{+9}_{-6}	N	...	...	...	...	0.72	$2.9^{+1.3}_{-1.0}$
IC 3779	$0.27^{+0.10}_{-0.08}$	$3.49^{+3.03}_{-2.06}$	15^{+6}_{-5}	N	...	...	...	...	0.66	$5.7^{+2.5}_{-1.8}$
NGC 4694	$1.94^{+0.40}_{-0.30}$	$3.02^{+1.82}_{-0.98}$	687^{+158}_{-115}	Y	$1.93^{+0.65}_{-0.48}$	$1.79^{+0.50}_{-0.38}$	0.65	0.83	...	$12.0^{+2.8}_{-2.0}$
NGC 4710	$6.94^{+2.03}_{-1.74}$	$2.09^{+0.69}_{-0.58}$	1004^{+381}_{-307}	Y	$7.38^{+1.75}_{-1.99}$	$5.70^{+3.35}_{-1.52}$	0.69	1.12	...	$10.6^{+4.0}_{-3.2}$
NGC 4733	$2.52^{+1.25}_{-0.97}$	$2.81^{+2.29}_{-1.42}$	90^{+61}_{-38}	Y	$1.60^{+1.32}_{-0.79}$	$2.41^{+1.01}_{-0.91}$	0.73	1.12	...	$3.2^{+2.2}_{-1.3}$
NGC 4754	$1.07^{+0.20}_{-0.15}$	$1.24^{+0.55}_{-0.41}$	130^{+29}_{-23}	Y	$1.64^{+0.93}_{-0.41}$	$1.11^{+0.29}_{-0.19}$	0.75	1.03	...	$1.1^{+0.3}_{-0.2}$
NGC 4762	$1.52^{+0.57}_{-0.29}$	$2.35^{+0.89}_{-0.59}$	321^{+102}_{-75}	Y	$2.88^{+1.90}_{-1.06}$	$0.99^{+0.19}_{-0.14}$	0.67	0.90	...	$1.4^{+0.4}_{-0.3}$
NGC 5839	$0.53^{+0.07}_{-0.07}$	$1.79^{+0.09}_{-0.11}$	34^{+9}_{-8}	N	...	...	...	...	0.85	$1.0^{+0.3}_{-0.2}$
NGC 5846	$4.97^{+0.05}_{-0.06}$	$1.69^{+0.06}_{-0.04}$	3198^{+139}_{-73}	Y	$3.60^{+0.26}_{-0.29}$	$2.04^{+0.10}_{-0.10}$	0.75	1.01	...	$12.1^{+0.5}_{-0.3}$
NGC 5866	$1.36^{+0.92}_{-0.44}$	$7.33^{+0.45}_{-0.80}$	383^{+89}_{-81}	Y	$2.64^{+1.46}_{-0.83}$	$0.59^{+0.38}_{-0.21}$	0.76	1.05	...	$2.2^{+0.5}_{-0.5}$
PGC 058114	$0.65^{+1.03}_{-0.48}$	$2.29^{+3.60}_{-1.61}$	20^{+29}_{-17}	N	...	...	...	...	0.65	$1.0^{+1.4}_{-0.8}$
NGC 6548	$0.26^{+0.54}_{-0.16}$	$5.84^{+1.60}_{-2.59}$	9^{+23}_{-7}	N	...	...	...	...	*nan*	$0.1^{+0.3}_{-0.1}$
NGC 7280	$0.29^{+1.25}_{-0.18}$	$2.09^{+2.92}_{-1.44}$	8^{+29}_{-6}	N	...	...	...	...	*nan*	$0.2^{+0.6}_{-0.1}$
NGC 7332	$0.60^{+0.18}_{-0.18}$	$0.98^{+1.47}_{-0.62}$	117^{+47}_{-32}	Y	$1.23^{+1.15}_{-0.43}$	$0.72^{+0.19}_{-0.30}$	0.77	0.96	...	$0.9^{+0.4}_{-0.2}$
NGC 7457	$1.07^{+0.49}_{-0.27}$	$4.12^{+2.69}_{-2.22}$	164^{+59}_{-50}	N	...	...	...	...	0.80	$4.4^{+1.6}_{-1.4}$
NGC 7454	$1.23^{+0.84}_{-0.41}$	$5.86^{+1.52}_{-2.62}$	96^{+46}_{-36}	N	...	...	...	...	0.97	$2.2^{+1.1}_{-0.8}$

Note. Column (1) lists the names of the galaxies. Columns (2) and (3) present the effective radii and Sérsic indices (n) of the GC systems, respectively. Column (4) shows the total number of GCs, and column (5) indicates the status of bimodality in the GC color distributions. Columns (6) to (9) detail the properties of GC systems with bimodal color distributions: effective radii of blue and red GC systems (columns (6) and (7)), and peak colors of blue and red GC systems (columns (8) and (9)). For unimodal GC color distributions, column (9) lists their median GC colors. Finally, column (11) shows the GC specific frequencies.

FoV. However, at the lower end of the number scale, the discrepancy between the two studies persists even with similar area coverage, indicating that the different coverages of both studies do not account for this difference.

We investigated additional factors that could contribute to these differences. In the case of several low-mass galaxies, GC numbers were estimated under specific conditions. In the ACSVCS, additional background fields were used to account for background

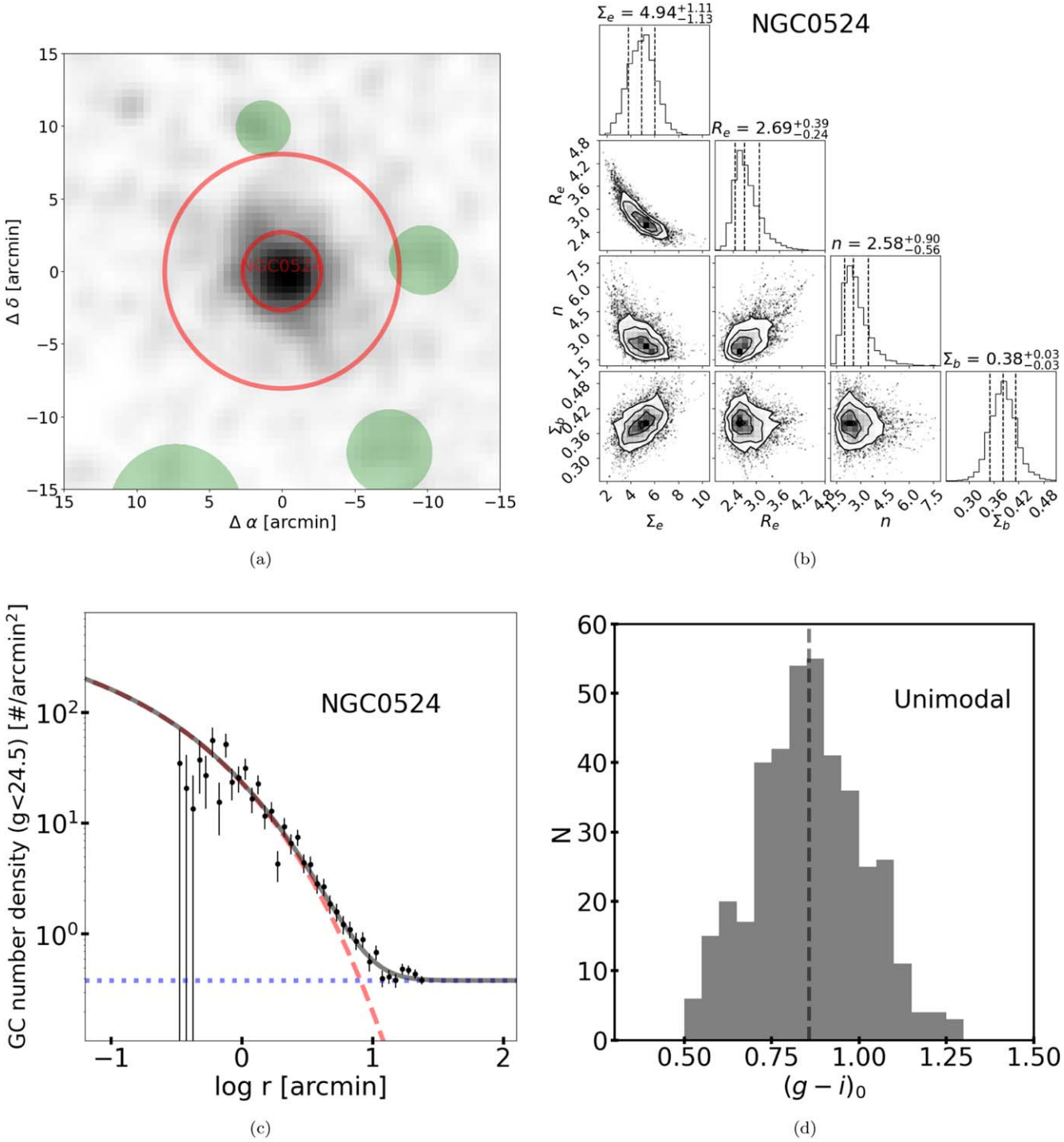

Figure 3. (a) Number density map of GC candidates in the NGC 524 region. The color bar is on logarithmic scale. Red circles represent $1R_{e,GC}$ and $3R_e$, *GC*, respectively. Green shaded areas show the masked regions; (b) two-dimensional and marginalized posterior probability density functions for the number density at the effective radius (Σ_e), the effective radius of the GC system (R_e), Sérsic index (n), and constant background (Σ_b). The vertical lines represent 15th, 50th, and 84th quartiles from left to right; (c) one-dimensional radial number density profile of GC candidates. Logarithmic bins are used. The black solid, red dashed, and blue dotted curves show the total function, Sérsic function, and constant background, respectively; (d) $(g - i)_0$ color distribution of GCs within $2R_{e,gc}$ of NGC 524. This distribution is categorized as a unimodal distribution by GMM. The black dashed line shows the median GC color.

(The complete figure set (50 images) is available in the online article.)

contamination when estimating GC numbers. However, for several low-mass galaxies, a local background was employed instead. These galaxies are marked with cyan circles in the right panel of Figure 8. In our GC number estimation, we used the fitted GCLFs from the ACSVCS for GCLF correction. However, there were a couple of galaxies in the ACSVCS for which GCLF information was unavailable. In these cases, we used the relation between GCLF and the host galaxy luminosity, marked with red in the right panel of Figure 8. About half of the low-GC-number galaxies had special conditions for GC number estimation in the ACSVCS. This suggests that the discrepancy in the number of low-GC galaxies may be due to these special conditions.

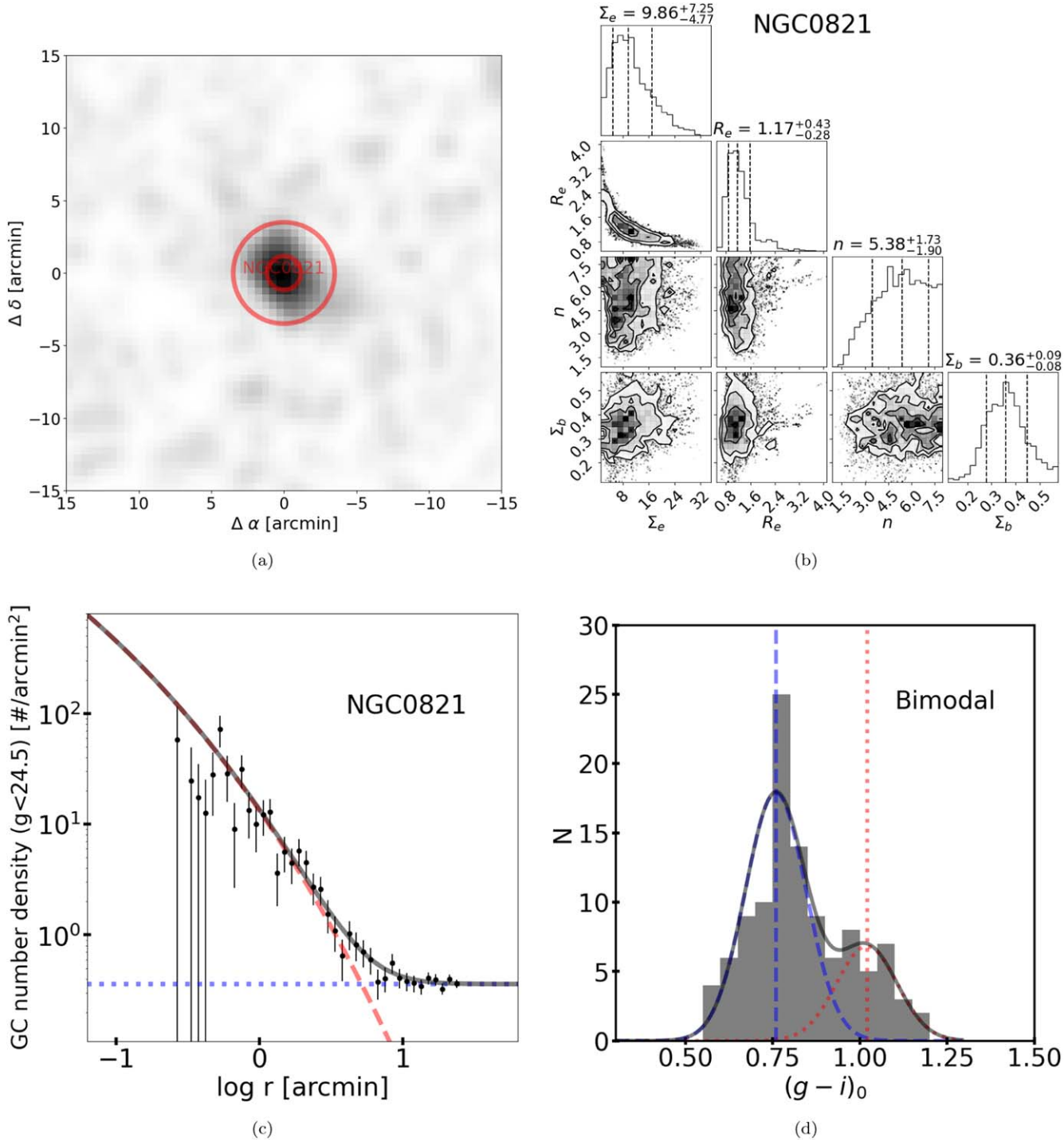

Figure 4. (a) Number density map of GC candidates in the NGC 821 region. The color bar is on logarithmic scale. Red circles represent $1R_{e,GC}$ and $3R_e$, *GC*, respectively. Green shaded areas show the masked regions, but there is no masked region in NGC 821; (b) two-dimensional and marginalized posterior probability density functions for the number density at the effective radius (Σ_e), the effective radius of the GC system (R_e), Sérsic index (n), and constant background (Σ_b). The vertical lines represent 15th, 50th, and 84th quartiles from left to right; (c) one-dimensional radial number density profile of GC candidates in NGC 821 region. The logarithmic bins are used. The black solid, red dashed, and blue dotted lines show the total function, Sérsic function, and constant background, respectively; (d) $(g-i)_0$ color distribution of GCs within $2R_{e,gc}$ in NGC 821. This distribution is categorized as a bimodal distribution by GMM. The blue dashed, red dotted, and black solid curves show fitted Gaussian functions of blue, red, and combined GCs, respectively. The vertical blue dashed and red dotted curves represent peak values of blue and red GC populations, respectively.

(The complete figure set (67 images) is available in the online article.)

There remain, however, several low-mass galaxies with discrepancies in GC numbers even when particular conditions are not involved. It is challenging to verify the cause of these discrepancies. We must delve into the differences in GC selection methods between the two studies to gain more insight. In our study, we used color–color and size information for GC selection. Additionally, we extended the maximum size limit for Virgo galaxies. The GC selection process used in the ACSVCS is more

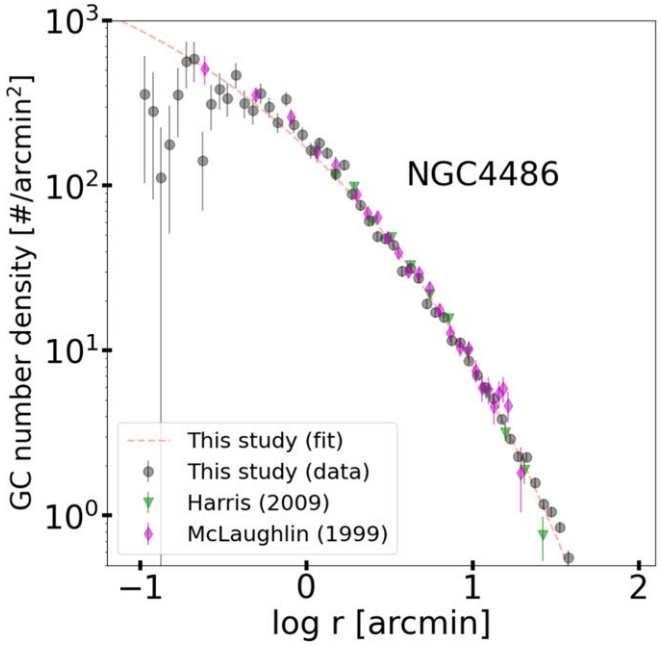

Figure 5. Comparison of the GC number density profile in NGC 4486 with the literature. *X*-axis is the radial distance from the center of NGC 4486, and *Y*-axis is the GC number density. Gray circles and red dashed line show data points and fitted results from this study. For comparison with previous studies, the background is subtracted, and the effect of the magnitude limit is corrected with the GCLF for GC number density. Magenta diamond and green inverted triangle represent results from D. E. McLaughlin (1999) and W. E. Harris (2009), respectively.

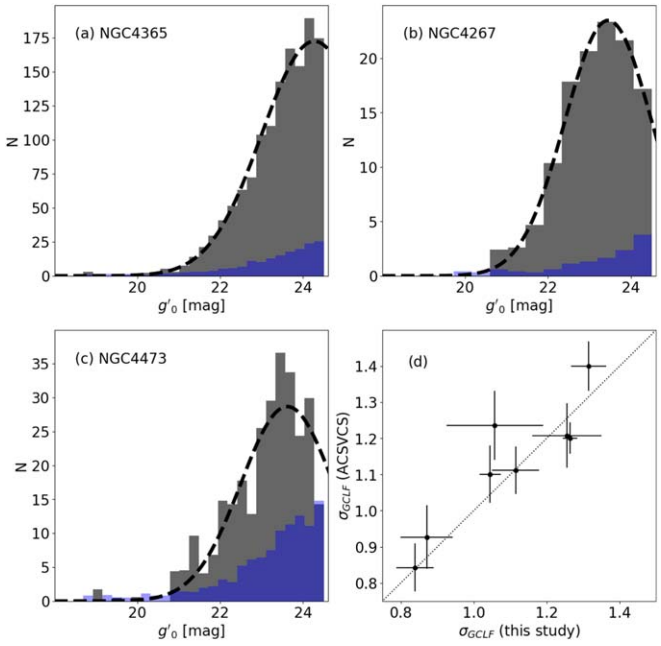

Figure 6. GC luminosity functions and their fitting results, with the fixed peak magnitude of the Gaussian function. (a) GCLF of NGC 4365. The gray histogram shows the background-subtracted GCLF, and the blue histogram represents the background. GCs are within $2R_{e,GCS}$, and the background area is chosen between $5R_{e,GCS}$ and $8R_{e,GCS}$. The dashed line represents the fitted Gaussian function with a fixed peak magnitude. (b) GCLF of NGC 4267, with notations the same as in panel (a). (c) GCLF of NGC 4473, with notations also the same as in panel (a). (d) Comparison of GCLF widths from this study and D. Villegas et al. (2010). The *X*- and *Y*-axes show σ_{GCLF} from this study and D. Villegas et al. (2010), respectively. The dotted line indicates a one-to-one correspondence.

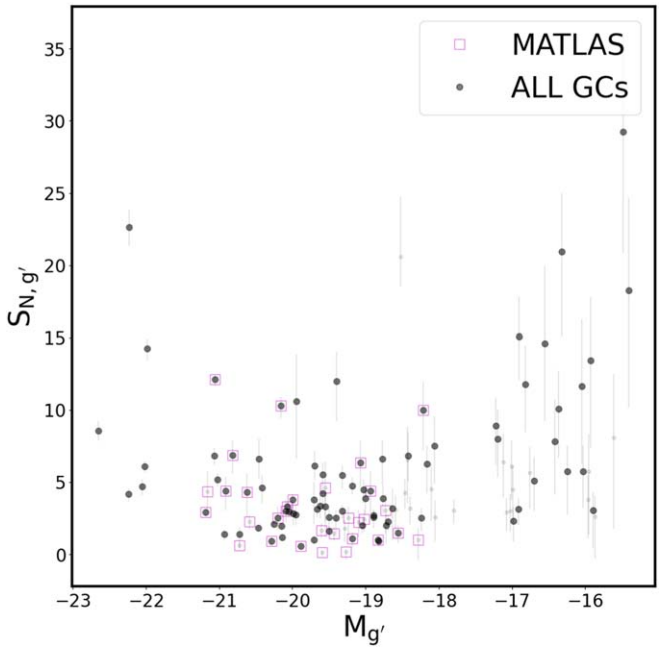

Figure 7. The GC specific frequencies ($S_{N,g'}$) are plotted against the absolute g'-band magnitudes of their host galaxies. Gray filled circles show GC systems from this study; well-fitted systems (error of $R_{e,gc} < 50\%$) are shown with large heavy symbols, and MATLAS galaxies are highlighted.

complicated than this study. They define the GC probability with color, size, and shape information. Based on this GC probability, they could identify clean GCs within specific color ranges and round, compact, but resolved sources. However, recent studies indicate that GCs can exhibit larger sizes and elongated shapes (e.g., P. R. Durrell et al. 2014; P. van Dokkum et al. 2018), potentially leading the ACSVCS survey to exclude some genuine GCs. This study included large GCs and did not consider ellipticity in GC selection, which should result in more complete GC samples than the ACSVCS. This effect of unusual GCs may be particularly significant in galaxies with fewer GCs.

3.3. Comparison of the Effective Radii with the Literature

Previous studies have reported effective radii for the GC systems in some of our program galaxies. Figure 9 compares the effective radii for GC systems from the literature with those measured in this study. Generally speaking, our measurements are consistent with those in the literature, albeit with some scatter. There are, however, slight differences between some individual literature measurements. In literature studies examining multiple galaxies, the findings of S. S. Kartha et al. (2014, 2016) show two cases consistent with our results and one notable discrepancy. The outlier is NGC 3608, which has a nearby companion galaxy, NGC 3607, with a GC system approximately twice as large as that of NGC 3608. S. S. Kartha et al. (2014, 2016) separated the GCs of the two galaxies based on their spatial locations and fit their distributions independently. However, as the GCs from both galaxies overlap in spatial extent, a simultaneous fitting approach we employed in this study is necessary for more accurate results. B. J. De Bórtoli et al. (2022) results also exhibit considerable divergence from ours, primarily due to three galaxies with the largest GC systems in their study and one with a notably smaller GC system than observed in our analysis. The largest GC system

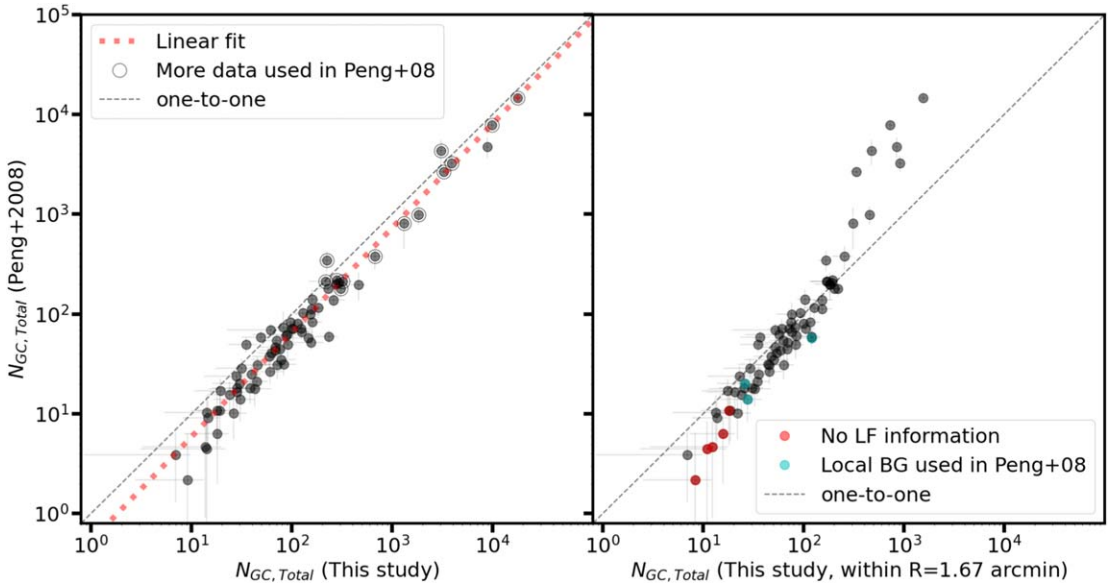

Figure 8. Comparison of $N_{GC,total}$ from the ACSVCS results (E. W. Peng et al. 2008) with this study. Left panel: Direct comparison of the total number of GCs from between this study and ACSVCS. The black dashed line and the red dotted line show the one-to-one relation and the linear fit, respectively. E. W. Peng et al. (2008) used additional data to fit GC density profiles for several galaxies because of large spatial distribution of GCs, and we mark them with large open circles. Right panel: Similar to the left panel, but total numbers of GCs in this study are limited within $1.'67$ similar to the ACS/WFC field of view. The dashed line shows the one-to-one relation. E. W. Peng et al. (2008) used additional background observations to estimate the number of GCs, but they used local background (in an ACS/WFC field) for several galaxies, so these galaxies are marked with cyan filled circles. This study uses Gaussian functions of the ACSVCS GCLF to correct for the magnitude limit, but several ACSVCS galaxies do not have a Gaussian form of the GCLF, so we have marked them with red filled circles.

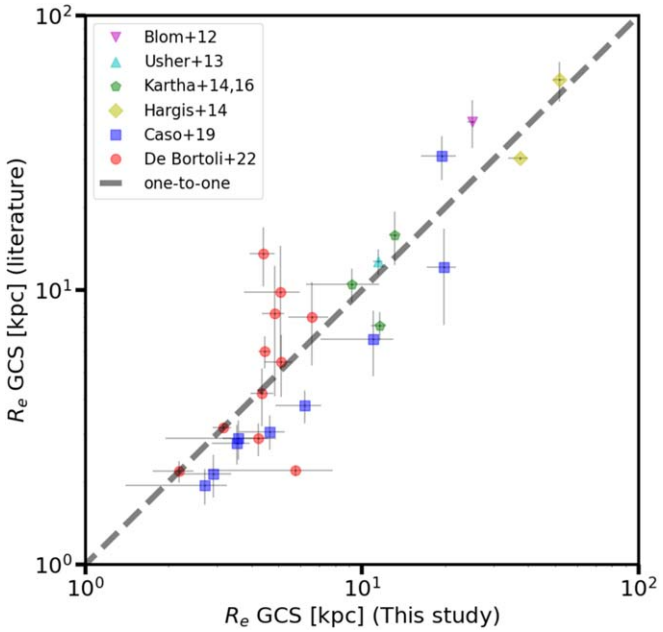

Figure 9. Comparison of $R_{e,gc}$ from literature with this study. The downward triangle shows NGC 4365 (C. Blom et al. 2012); the triangle shows NGC 4278 (C. Usher et al. 2013), and pentagons show three galaxies from the SLUGGS survey (S. S. Kartha et al. 2014, 2016), diamonds, NGC 4472 and NGC 4406 (J. R. Hargis & K. L. Rhode 2014), squares (J. P. Caso et al. 2019), and circles (B. J. De Bórtoli et al. 2022).

reported by B. J. De Bórtoli et al. (2022) is for NGC 4435, which has a nearby companion that may contribute additional GCs, thus increasing the size of the GC system. The two other large GC systems in B. J. De Bórtoli et al. (2022) show substantial uncertainties in size estimation, leading us to consider our estimates more reliable. Additionally, the smallest GC system reported by B. J. De Bórtoli et al. (2022) may be influenced by the limited spatial coverage of their data, an issue similarly noted in comparison with results from J. P. Caso et al. (2019).

4. Summary

We investigate the spatial distribution of GCs belonging to 118 ETGs using imaging data from the NGVS, and the MATLAS, supplemented by the ACS Virgo Cluster Survey for central galaxy regions, when available. Our program, along with a companion paper, aims to understand the connection between galaxy evolution and GC system size, focusing on the effective radii of GC systems and their correlation with various galaxy properties (S. Lim et al. 2024).

Photometry is performed on model-subtracted galaxy images to detect GC candidates. Aperture magnitudes are used to estimate source fluxes, with corrections made for fixed aperture size limitations using the largest available aperture. We select GC candidates based on both size/concentration and two-color information, considering both pointlike and slightly extended sources.

Completeness tests are carried out by injecting approximately 200,000 artificial stars into each field. The recovery rate for the brighter than $m_g = 24.5$ mag is almost 100% across the overall field except for the central regions of bright galaxies.

Spatial distributions of GCs are modeled using modified two-dimensional Sérsic profiles. Our fitting procedure employs the MCMC method, explicitly utilizing the emcee code in Python. In cases where neighboring galaxies harbor a significant GC population, a simultaneous fitting with two Sérsic functions is applied. We estimate the total number of GCs by integrating the Sérsic profiles and correcting for the GCLF.

Furthermore, GCs are categorized into subsamples based on their colors using the GMM. More than half of the sample (68)

show bimodality in GC color distribution. Spatial distributions of these subsamples are also subjected to fitting.

This study represents the largest and most homogeneous sample to date for studying the spatial distributions of GC systems. A companion paper (S. Lim et al. 2024) provides the scientific outcomes from the data and catalogs described in this paper. In a future paper, we plan to extend the analysis to include dwarf galaxies outside galaxy cluster environments, explicitly focusing on investigating the GC spatial distributions for dwarf galaxies using MATLAS data. Euclid will soon provide a large database as well.

Acknowledgments

S.L. acknowledges the support from the Sejong Science Fellowship Program by the National Research Foundation of Korea (NRF) grant funded by the Korea government (MSIT; No. NRF-2021R1C1C2006790). C.L. acknowledges support from the National Natural Science Foundation of China (NSFC, grant Nos. 12173025, 11833005, 11933003), 111 project (No. B20019), and Key Laboratory for Particle Physics, Astrophysics and Cosmology, Ministry of Education. C.S. acknowledges support from ANID/CONICYT through FONDECYT Postdoctoral Fellowship Project No. 3200959. A.L. and P.A.D. acknowledge support from Agence Nationale de la Recherche, France, under project ANR-19-CE31-0022. O.M. is grateful to the Swiss National Science Foundation for financial support under grant No. PZ00P2_202104.

IRAF was distributed by the National Optical Astronomy Observatory, which was managed by the Association of Universities for Research in Astronomy (AURA) under a cooperative agreement with the National Science Foundation. Based on observations obtained with MegaPrime/MegaCam, a joint project of CFHT and CEA/DAPNIA, at the Canada–France–Hawaii Telescope (CFHT), which is operated by the National Research Council (NRC) of Canada, the Institut National des Science de l'Univers of the Centre National de la Recherche Scientifique (CNRS) of France, and the University of Hawaii. The observations at the Canada–France–Hawaii Telescope were performed with care and respect from the summit of Maunakea, which is a significant cultural and historic site.

This research is based on observations made with the NASA/ESA Hubble Space Telescope obtained from the Space Telescope Science Institute, which is operated by the Association of Universities for Research in Astronomy, Inc., under NASA contract NAS 5-26555. These observations are associated with program GO-9401. This research was supported by the International Space Science Institute (ISSI) in Bern, through ISSI International Team project No. 534 (Space Observations of Dwarf Galaxies from Deep Large Scale Surveys: The MATLAS Experience).

Some of the data presented in this paper were obtained from the Mikulski Archive for Space Telescopes (MAST) at the Space Telescope Science Institute. The specific observations analyzed can be accessed via DOI: 10.17909/yc2t-rr81.

Facilities: HST (ACS), CFHT.

Software: astropy (Astropy Collaboration et al. 2013, 2018, 2022), Source Extractor (E. Bertin & S. Arnouts 1996).

Appendix
Notes for All Samples

1. *NGC 524.* The GC spatial distribution is well fitted by the Sérsic function. Interestingly, it shows a unimodal GC color distribution even though it is a fairly massive galaxy. The central region of this galaxy is studied with HST (A. Kundu & B. C. Whitmore 2001a), and the GC color distribution in the HST study is similar to that of this study. It is notable that a previous spectroscopic study has demonstrated that metal-poor GCs exhibit distinct kinematics when compared to metal-rich GCs (M. A. Beasley et al. 2004). To confirm the existence of GC subpopulations, further spectroscopic observations of GCs are necessary.
2. *NGC 821.* The GC spatial distribution is well fitted by the Sérsic function with a high Sérsic index. The number of GCs ($N_{GC} = 764^{+315}_{-230}$) in this study is larger than twice of those in the literature ($N_{\rm GC} = 395 \pm 94$, A. Kundu & B. C. Whitmore 2001b; $N_{\rm GC} = 320 \pm 54$, L. R. Spitler et al. 2008). This discrepancy may be attributed to differences in the coverage and depth of observation. The radial number density profile of GCs in the literature reaches a background level at approximately 3', whereas our findings indicate an excess of GCs up to 10′.
3. *NGC 936.* GCs are more centrally concentrated than other galaxies.
4. *NGC 1023.* The GC spatial distribution is elongated. The GC system in this galaxy has been studied in several pieces of literature (S. S. Larsen & J. P. Brodie 2000; M. D. Young et al. 2012; S. S. Kartha et al. 2014; D. de Brito Silva 2022). The number of GCs in this study is slightly smaller than that reported in the literature. The reason for this discrepancy is not immediately apparent. However, it is possible that it may be due to differences in the fitting of radial profiles.
5. *NGC 2592.* There is a background galaxy (NGC 2594, 35.1Mpc) to the southwest of NGC 2592. We masked out this region instead of fitting it simultaneously because of its different distance.
6. *NGC 2685.* The GC number density peak is offset from the galaxy center.
7. *NGC 2768.* The Sérsic function with a high Sérsic index fits the GC spatial distribution well. This galaxy is studied in S. S. Kartha et al. (2014), and the effective radius of the GC system is consistent, but the number of GCs in this study is ~40% larger than that in S. S. Kartha et al. (2014).
8. *NGC 2778.* The GC spatial distribution has a long tail to the north. The GC color distribution is determined to be bimodal by statistical testing, but the red population is very small.
9. *NGC 2950.* The blue and red GC populations are comparable.
10. *NGC 3098.* The GC number density peak is offset from the galaxy center. The blue and red peaks of GCs are relatively bluer than those of other galaxies.
11. *NGC 3245.* The GC color distribution is unimodal, but has a peak in blue and a tail in red.
12. *NGC 3379.* It has a neighbor, NGC 3384, so we fit two Sérsic functions simultaneously. The fitted Sérsic index is close to 8, which is our upper limit for the Sérsic index. The blue and red GC populations are comparable. This galaxy is studied in K. L. Rhode & S. E. Zepf (2004), and the total number of GCs is comparable in both studies.
13. *NGC 3384.* It has a neighbor, NGC 3384, so we fit two Sérsic functions simultaneously. Interestingly, its fitted

Sérsic index is about 0.5, which is close to our lower limit for the Sérsic index. The red GC population is larger than the blue GC population. J. R. Hargis & K. L. Rhode (2012) studied this galaxy, and their result for the total number of GCs is consistent with this study.

14. *NGC 3457.* There is no special feature in GC properties.
15. *NGC 3489.* The GC color distribution is very clearly bimodal, and the color of red GCs is redder than that of other galaxies. A. Kundu & B. C. Whitmore (2001a) studied the central region of this galaxy with the HST, but it is difficult to find distinguished red GCs in this literature.
16. *NGC 3599.* There is no special feature in GC properties. The central region of this galaxy is studied by A. Kundu & B. C. Whitmore (2001a) with the HST.
17. *NGC 3607.* It has a neighbor, NGC 3608, so we fit two Sérsic functions simultaneously. The fitted Sérsic index is close to 8, which is our upper limit for the Sérsic index. S. S. Kartha et al. (2016) has studied this galaxy, and their $R_{e,gc}$ is consistent with this study, but their Sérsic index is much smaller than ours. GCs in the central region were studied in A. Kundu & B. C. Whitmore (2001a).
18. *NGC 3608.* It has a neighbor, NGC 3607, so we fit two Sérsic functions simultaneously. S. S. Kartha et al. (2016) has studied this galaxy, and their $R_{e,gc}$ is a little smaller than this study. GCs in the central region were studied in A. Kundu & B. C. Whitmore (2001b).
19. *NGC 3630.* GCs are more centrally concentrated than other galaxies.
20. *NGC 3945.* The GC number density peak is offset from the galaxy center.
21. *IC 3032.* The GC number density peak is offset from the galaxy center. We have a larger total number of GCs than that in the ACSVCS (E. W. Peng et al. 2008). Please check Section 3.2.
22. *IC 3065.* The GC number density peak is offset from the galaxy center. The total number of GCs is about twice that in the ACSVCS (E. W. Peng et al. 2008). Please check Section 3.2.
23. *VCC 200.* The GC number density peak is offset from the galaxy center. The total number of GCs is consistent with that in the ACSVCS (E. W. Peng et al. 2008).
24. *IC 3101.* There is no special feature in GC properties. The total number of GCs is consistent with that in the ACSVCS (E. W. Peng et al. 2008).
25. *NGC 4262.* A small neighboring galaxy is in the field, so we masked that region. K. R. Akhil et al. (2024) have studied GC properties using the same data as this study, but their $R_{e,gc}$ differs slightly from that in this study. This may be due to different analysis methods, including different magnitude limits and fitting methods (binned data versus individual data points).
26. *NGC 4267.* The GC number density profile is flattened in the central region. It has a large population of red GCs. B. J. De Bórtoli et al. (2022) studied the $R_{e,gc}$ of this galaxy, but their $R_{e,gc}$ is slightly larger than in this study, which could be due to different data (HST only versus combined HST and CFHT).
27. *NGC 4278.* It has a neighbor, NGC 4283, so we fit two Sérsic functions simultaneously. Interestingly, $R_{e,\mathrm{BGC}}$ is much smaller than $R_{e,gc}$, which could be due to the extremely large $R_{e,\mathrm{BGC}}$ of its neighbor, NGC 4283. Although there is a high possibility of underestimating $R_{e,\mathrm{BGC}}$ for NGC 4278 (and conversely, overestimating $R_{e,\mathrm{BGC}}$ for NGC 4283), we keep these results to maintain consistency in estimating $R_{e,gc}$ for all samples. C. Usher et al. (2013) have investigated the GC properties of this study. Their $R_{e,gc}$ is in agreement with this study.
28. *NGC 4283.* It has a neighbor, NGC 4278, so we fit two Sérsic functions simultaneously. Please check the note for NGC 4278.
29. *UGC 7436.* GCs are more centrally concentrated than other galaxies. It is included in P. R. Durrell et al. (1996), and they provided a smaller total number of GCs ($N_{\mathrm{GC}} = 20 \pm 11$) compared to that of this study, but it is consistent with ours within the margin of error. The total number of GCs in this study is larger than that in the ACSVCS ($N_{\mathrm{GC}} = 18.1 \pm 5.5$, E. W. Peng et al. 2008). Please check Section 3.2 for this discrepancy.
30. *VCC 571.* GCs are rarely detected. The total number of GCs is slightly larger than that in the ACSVCS (E. W. Peng et al. 2008). Please check Section 3.2.
31. *NGC 4318.* GC color distribution is bimodal even with a very small number of GCs, and this bimodality was also shown in E. W. Peng et al. (2006).
32. *NGC 4339.* There is no special feature in GC properties.
33. *NGC 4340.* It has a neighbor, NGC 4350, so we fit two Sérsic functions simultaneously. The total number of GCs is slightly larger than that in the ACSVCS (E. W. Peng et al. 2008), but they are consistent within the margin of error.
34. *NGC 4342.* It has a neighbor, NGC 4365, so we fit two Sérsic functions simultaneously. The color distribution is bimodal, but blue and red peaks are very close. C. Blom et al. (2014) have studied GC properties of this galaxy, and their $R_{e,gc}$ and Sérsic index n values are consistent with this study.
35. *NGC 4350.* It has a neighbor, NGC 4340, so we fit two Sérsic functions simultaneously. The total number of GCs is larger than that in the ACSVCS (E. W. Peng et al. 2008). Please check Section 3.2.
36. *NGC 4352.* There is a bright star nearby, so its region is masked. The total number of GCs is consistent with that in the ACSVCS (E. W. Peng et al. 2008).
37. *NGC 4365.* It has a neighbor, NGC 4342, so we fit two Sérsic functions simultaneously. The blue and red GC populations are comparable. The GC system of this galaxy has been studied in many pieces of literature (e.g., D. A. Forbes 1996; A. Kundu & B. C. Whitmore 2001b; T. H. Puzia et al. 2002; J. P. Brodie et al. 2005; A. Kundu et al. 2005), and C. Blom et al. (2012) provide the fitting results for the GC spatial distribution. Their $R_{e,gc}$ and N_{GC} are much larger than those in this study. This discrepancy could be due to background estimation. They could not reach the edge of the GC spatial distribution in their observation, but we did. Additionally, they do not mention the effect of NGC 4342. If we fit the GC spatial distribution with a single Sérsic profile while masking out the NGC 4342 area, we obtain a slightly larger $R_{e,gc}$ than from a two Sérsic fit. Therefore, we expect that the $R_{e,gc}$ in the literature was overestimated due to the effect of the neighboring galaxy.

38. *NGC 4371.* There is no special feature in GC properties. B. J. De Bórtoli et al. (2022) provide $R_{e,gc}$, and it is much larger than that in this study. However, their $R_{e,gc}$ has a large error, so their $R_{e,gc}$ and that in this study are consistent within the margin of error.
39. *NGC 4374.* It has a neighbor, NGC 4406, so we fit two Sérsic functions simultaneously. There are other galaxies nearby, so we masked them out aggressively. There are several published works that provide N_{GC} of this galaxy (e.g., T. Richtler & T. Richtler 2004; E. W. Peng et al. 2008; R. A. Lambert et al. 2020). However, previous pieces of literature do not address the impact of NGC 4406 due to limit of data, suggesting that our result could be the most reliable.
40. *NGC 4377.* The blue and red GC populations are comparable, but it is not shown in the ACSVCS (E. W. Peng et al. 2006). B. J. De Bórtoli et al. (2022) shows $R_{e,gc}$ of this galaxy, and it is consistent with this study.
41. *NGC 4379.* There is no special feature in GC properties. The central region was investigated using HST data in A. Kundu & B. C. Whitmore (2001a), but the resulting N_{GC} values are considerably smaller due to the limitations of the HST spatial coverage.
42. *NGC 4387.* There are two big neighbors. Because both galaxies seem to affect equally, it is difficult to choose one of them for dual Sérsic fit, so we masked them out. Total numbers of GCs from literatures (E. W. Peng et al. 2008; R. A. Lambert et al. 2020) are consistent with our result, and $R_{e,gc}$ from J. P. Caso et al. (2019) is also consistent with our result.
43. *IC 3328.* There is no special feature in GC properties.
44. *NGC 4406.* It has a neighbor, NGC 4374, so we fit two Sérsic functions simultaneously. There are other galaxies nearby, so we masked them out aggressively. N_{GC} from this study is slightly larger than those in the literature ($N_{GC} = 2900 \pm 400$ K. L. Rhode & S. E. Zepf 2004; R. A. Lambert et al. 2020; $N_{GC} = 2660 \pm 129$, E. W. Peng et al. 2008), and it may be due to the limited spatial coverage of previous studies. J. R. Hargis & K. L. Rhode (2014) estimated $R_{e,gc} = 5\farcm8 \pm 0\farcm1$ with Sérsic function fitting, which is smaller than our result. They also provide an empirical $R_{e,gc} = 6\farcm4$, which is still slightly smaller than our result. This discrepancy may be due to differences in the approach to handling neighboring galaxies.
45. *NGC 4417.* It has a neighbor, NGC 4424, so we fit two Sérsic functions simultaneously. B. J. De Bórtoli et al. (2022) estimated $R_{e,gc}$ of this galaxy, which is consistent with that in this study.
46. *NGC 4425.* It has a neighbor, NGC 4406, so we fit two Sérsic functions simultaneously.
47. *NGC 4429.* It has a bimodal GC color distribution, but there is a peak in the middle of the blue and red GCs.
48. *NGC 4434.* There is a bright star nearby, so its region is masked. N_{GC} and $R_{e,gc}$ from previous studies (E. W. Peng et al. 2008; J. P. Caso et al. 2019) are smaller than those in this study. It may be due to the limited spatial coverage of previous studies.
49. *NGC 4435.* The west side is close to NGC 4406, and there is significant background contamination on the east side, so we aggressively masked it out. It has a neighbor, NGC 4438, so we fit two Sérsic functions simultaneously. It is interesting that N_{GC} and $R_{e,gc}$ from previous studies (E. W. Peng et al. 2008; B. J. De Bórtoli et al. 2022) are larger than those in this study. This discrepancy may be due to the different methods employed in dealing with the background and neighbor galaxies.
50. *NGC 4442.* The GC spatial distribution is elongated. The blue and red GC populations are comparable, while this galaxy has no particular high red GC fraction in the ACSVCS (E. W. Peng et al. 2006). N_{GC} from the ACSVCS (E. W. Peng et al. 2008) is smaller than that in this study, and it could be due to the small areal coverage of the ACSVCS. $R_{e,gc}$ from the previous study ($R_{e,gc} = 1\farcm8 \pm 0\farcm9$, B. J. De Bórtoli et al. 2022) is much larger than our result, but both are consistent within the margin of error.
51. *IC 3383.* There is a neighbor dwarf galaxy at north, so we masked it out.
52. *IC 3381.* There is no special feature in GC properties.
53. *NGC 4452.* There is a neighboring dwarf galaxy and a bright star, so we masked them out.
54. *NGC 4458.* We rigorously masked out due to three nearby bright neighbors. N_{GC} in this study is a little larger than those in the previous studies (A. Kundu & B. C. Whitmore 2001b; E. W. Peng et al. 2008), and it may be due to the limited spatial coverage of the previous studies. $R_{e,gc}$ in the previous study (J. P. Caso et al. 2019) is consistent with that in this study.
55. *NGC 4459.* The blue and red GC populations are comparable, while this galaxy has no particular high red GC fraction in the ACSVCS (E. W. Peng et al. 2006). N_{GC}. N_{GC} in the ACSVCS is a little smaller than our result. $R_{e,gc}$ in the previous study (B. J. De Bórtoli et al. 2022) is consistent with that in this study.
56. *NGC 4461.* It has a neighbor, NGC 4458, so we fit two Sérsic functions simultaneously, but it also has a large neighbor to the northeast. We masked it out.
57. *VCC 1185.* There is no special feature in GC properties. This galaxy was studied in P. R. Durrell et al. (1996), and their total number of GCs ($N_{GC} = 7 \pm 9$) is smaller than our result. This discrepancy could be due to the limited spatial coverage of the previous study. The ACSVCS also studied this galaxy with a slightly smaller total number of GCs ($N_{GC} = 14 \pm 5.7$) than that in this study, but they are consistent within the margin of error.
58. *NGC 4472.* It has a neighbor, NGC 4365, so we fit two Sérsic functions simultaneously. Other small neighbors and contaminations are masked out. The GC system of this galaxy has been studied in many pieces of literature (e.g., M. G. Lee et al. 1998; K. L. Rhode & S. E. Zepf 2001; P. Côté et al. 2003). J. R. Hargis & K. L. Rhode (2014) estimated $R_{e,GC}$ with a Sérsic profile, and their result ($R_{e,gc} = 12' \pm 2'$) is consistent with that in this study. The total number of GCs in the ACSVCS ($N_{GC} = 7813 \pm 830$, E. W. Peng et al. 2008) is slightly smaller than that in this study. This discrepancy may be due to different ways of estimating the background and effect of neighbor galaxies.
59. *NGC 4473.* There is no special feature in GC properties. Several previous studies estimated the total number of GCs. However, their results are smaller than that in this study mainly due to the small areal coverage of the previous studies (A. Kundu & B. C. Whitmore 2001b; S. S. Larsen et al. 2001; E. W. Peng et al. 2008).
60. *NGC 4474.* There is no special feature in GC properties. B. J. De Bórtoli et al. (2022) estimated $R_{e,gc}$, and their

result ($R_{e,gc}$ = 0.″64 ± 0.″09) is slightly smaller than our result. N_{gc} from the ACSVCS (N_{gc} = 116 ± 24) is also slightly smaller than our result. Both discrepancies could be due to small areal coverage of previous studies.

61. *NGC 4476.* It has a huge neighbor, NGC 4486, so we fit two Sérsic functions simultaneously. The N_{GC} of this galaxy in the ACSVCS is slightly smaller than our result, but both are consistent within the margin of error.
62. *NGC 4477.* It has a huge neighbor, NGC 4473, so we fit two Sérsic functions simultaneously.
63. *NGC 4482.* There is no special feature in GC properties. N_{GC} from the ACSVCS (E. W. Peng et al. 2008) is smaller than that in this study, and it could be due to the small areal coverage of the ACSVCS.
64. *NGC 4478.* It has a huge neighbor, NGC 4486, so we fit two Sérsic functions simultaneously. N_{GC} from the ACSVCS (E. W. Peng et al. 2008) is smaller than that in this study, and it could be due to ways of subtracting the contamination from the big neighbor.
65. *NGC 4479.* It has a neighbor, NGC 4473, so we fit two Sérsic functions simultaneously, but it also has a large contamination to the northwest. We masked it out. N_{GC} from the ACSVCS (E. W. Peng et al. 2008) is consistent with that in this study.
66. *NGC 4483.* There is no special feature in GC properties. B. J. De Bórtoli et al. (2022) estimated $R_{e,gc}$, and their result ($R_{e,gc}$ = 0.″45 ± 0.″02) is smaller than our result. N_{gc} from the ACSVCS (N_{gc} = 58.6 ± 9.3) is also smaller than our result. Both discrepancies could be due to small areal coverage of previous studies.
67. *NGC 4486.* It has a lot of neighbor galaxies, but we masked them out except for NGC 4406. We fit two Sérsic functions simultaneously. Our GC radial number density profile is consistent with previous studies (Figure 5). There are a lot of previous studies for the GC system of this galaxy, and the total number of GCs in the previous studies is about 14,000 − 15,000 (e.g., N. Tamura et al. 2006; E. W. Peng et al. 2008), but we have a little larger N_{GC}. It may be due to different spatial coverage.
68. *NGC 4489.* There is no special feature in GC properties. N_{GC} from the ACSVCS (E. W. Peng et al. 2008) is smaller than that in this study. Please check Section 3.2.
69. *IC 3461.* There is a bump on the outer edge of the GC radial number density profile. The GC system of this galaxy was studied in P. R. Durrell et al. (1996), and their N_{GC} (= 16 ± 12) is smaller than that of this study, but both results are consistent within the margin of error.
70. *NGC 4503.* It has a neighbor, IC 3470, so we fit two Sérsic functions simultaneously.
71. *IC 3468.* The blue and red GC populations are comparable, but blue and red peaks are close. N_{GC} from the ACSVCS (E. W. Peng et al. 2008) is smaller than that in this study. Please check Section 3.2.
72. *IC 3470.* There is no special feature in GC properties. N_{GC} from the ACSVCS (E. W. Peng et al. 2008) is smaller than that in this study. Please check Section 3.2.
73. *IC 798.* There is no special feature in GC properties. N_{GC} from the ACSVCS (E. W. Peng et al. 2008) is smaller than that in this study. Please check Section 3.2.
74. *NGC 4515.* There is no special feature in GC properties. $R_{e,gc}$ from the previous study ($R_{e,gc}$ = 0.″40 ± 0.″06, T. Carleton et al. 2019) is slightly smaller than our result, but they are consistent within the margin of error. N_{GC} from the ACSVCS (E. W. Peng et al. 2008) is smaller than that in this study. Please check Section 3.2.
75. *VCC 1512.* GCs are rarely detected. N_{GC} from the ACSVCS (E. W. Peng et al. 2008) is smaller than that in this study. Please check Section 3.2.
76. IC 3501. There are three bright stars nearby, so we masked them out. N_{GC} from the ACSVCS (E. W. Peng et al. 2008) is smaller than that in this study. Please check Section 3.2.
77. *NGC 4528.* There is a bright star in the east and a dwarf galaxy in the north, so we masked them out. N_{GC} from the ACSVCS (E. W. Peng et al. 2008) is smaller than that in this study. Please check Section 3.2.
78. *VCC 1539.* There is no special feature in GC properties. N_{GC} from the ACSVCS (E. W. Peng et al. 2008) is smaller than that in this study, but they are consistent within the margin of error. Please check Section 3.2.
79. *IC 3509.* There is no special feature in GC properties. N_{GC} from the ACSVCS (E. W. Peng et al. 2008) is smaller than that in this study, but they are consistent within the margin of error. Please check Section 3.2.
80. *NGC 4550.* It has a neighbor, NGC 4551, so we fit two Sérsic functions simultaneously. The blue and red GC populations are comparable, which is similar to the results in E. W. Peng et al. (2006). N_{GC} from previous studies (A. Kundu & B. C. Whitmore 2001b; E. W. Peng et al. 2008) are consistent with that in this study.
81. *NGC 4551.* It has a neighbor, NGC 4550, so we fit two Sérsic functions simultaneously. A large area at north is masked out due to a large neighbor galaxy. The blue and red GC populations are comparable, which is similar to the results in E. W. Peng et al. (2006). N_{GC} from the previous study (E. W. Peng et al. 2008) is consistent with that in this study.
82. *NGC 4552.* There are several dwarf galaxies nearby, so we masked them out. $R_{e,gc}$ from the previous study ($R_{e,gc}$ = 2.″6 ± 1.″0, T. Carleton et al. 2019) is much smaller than our result, and N_{GC} from the ACSVCS (E. W. Peng et al. 2008) is also smaller than that in this study. It may be due to the limited spatial coverage of previous studies. Please check Section 3.2.
83. *VCC 1661.* There is no special feature in GC properties. N_{GC} from the ACSVCS (E. W. Peng et al. 2008) is smaller than that in this study. Please check Section 3.2.
84. *NGC 4564.* There is a bright star in the west and a dwarf galaxy in the south, so we masked them out. The red GC population is larger than the blue GC population, which is already shown in the ACSVCS (E. W. Peng et al. 2006). $R_{e,gc}$ from the previous study ($R_{e,gc}$ = 0.″6 ± 0.″1, T. Carleton et al. 2019) is slightly smaller than our result, but they are consistent within the margin of error. N_{GC} from the ACSVCS (E. W. Peng et al. 2008) is consistent with that in this study.
85. *NGC 4570.* There is no special feature in GC properties. $R_{e,gc}$ from the previous study ($R_{e,gc}$ = 1.″6 ± 0.″5, B. J. De Bórtoli et al. 2022) is slightly larger than our result, but they are consistent within the margin of error. N_{GC} from the ACSVCS (E. W. Peng et al. 2008) is smaller than that in this study. Please check Section 3.2.
86. *NGC 4578.* There is a bright star in the east, so we masked it out. The N_{GC} of this galaxy in the ACSVCS

(E. W. Peng et al. 2008) is smaller than our result, but they are consistent within the margin of error.

87. *NGC 4596.* There is a bump on the outer edge of the GC radial number density profile.
88. *VCC 1826.* GCs are rarely detected. The $N_{\rm GC}$ of this galaxy in the ACSVCS (E. W. Peng et al. 2008) is smaller than our result, but they are consistent within the margin of error.
89. *VCC 1833.* The GC number density peak is offset from the galaxy center. The $N_{\rm GC}$ of this galaxy in the ACSVCS (E. W. Peng et al. 2008) is slightly smaller than our result, but they are consistent within the margin of error.
90. *IC 3647.* The GC color distribution is determined to be bimodal by statistical testing, although the number of GCs is small, and it was determined as an unimodal distribution in the ACSVCS (E. W. Peng et al. 2006). The $N_{\rm GC}$ of this galaxy in the ACSVCS is slightly smaller than our result, but they are consistent within the margin of error.
91. *IC 3652.* There is no special feature in GC properties. The $N_{\rm GC}$ of this galaxy in the ACSVCS (E. W. Peng et al. 2008) is smaller than our result, but they are consistent within the margin of error.
92. *NGC 4608.* The GC spatial distribution is elongated.
93. *IC 3653.* It has a neighbor, NGC 4621, so we fit two Sérsic functions simultaneously. The $N_{\rm GC}$ of this galaxy in the ACSVCS (E. W. Peng et al. 2008) is slightly smaller than our result, but they are consistent within the margin of error.
94. *NGC 4612.* This galaxy is on the edge of the NGVS footprint. $N_{\rm GC}$ from the ACSVCS (E. W. Peng et al. 2008) is much smaller than that in this study. Please check Section 3.2.
95. *VCC 1886.* GCs are rarely detected. The $N_{\rm GC}$ of this galaxy in the ACSVCS (E. W. Peng et al. 2008) is slightly smaller than our result, but they are consistent within the margin of error.
96. *UGC 7854.* The GC number density peak is offset from the galaxy center. The blue and red GC populations are comparable, but it was shown as an unimodal in the ACSVCS (E. W. Peng et al. 2006). The $N_{\rm GC}$ of this galaxy in the ACSVCS (E. W. Peng et al. 2008) is slightly smaller than our result, but they are consistent within the margin of error.
97. *NGC 4621.* It has a neighbor, NGC 4649, so we fit two Sérsic functions simultaneously. $R_{e,gc}$ from the previous study ($R_{e,gc} = 7\farcm1 \pm 1\farcm3$, T. Carleton et al. 2019) is larger than our result. $N_{\rm GC}$ from the ACSVCS (E. W. Peng et al. 2008) is smaller than that in this study. These discrepancies could be due to ways of subtracting the contamination from the big neighbor.
98. *NGC 4638.* It has a neighbor, NGC 4649, so we fit two Sérsic functions simultaneously. $N_{\rm GC}$ from the ACSVCS (E. W. Peng et al. 2008) is much smaller than that in this study. Please check Section 3.2.
99. *NGC 4649.* It has a neighbor, NGC 4621, so we fit two Sérsic functions simultaneously. The total number of GCs is 8875^{+508}_{-419}, which is twice the number reported in the literature ($N_{\rm GC} = 4745 \pm 1099$, ACSVCS; $N_{\rm GC} = 3700 \pm 900$, D. A. Forbes et al. 2004; $N_{\rm GC} = 3600 \pm 500$, M. G. Lee et al. 2008). This discrepancy is mainly due to background estimation. The background was defined in the literature as approximately $10'$ from the galaxy center, but we found that $R_{e,gc}$ is larger than $10'$ ($R_{e,gc} = 15\farcm71^{+0.41}_{-0.38}$). The excess of GCs over the background is very clear up to tens of arcminutes (Figure 4). However, the GC number density profile does not seem to fit well with a single Sérsic profile. There may be an additional component starting at approximately $10'$ radius. While we cannot confirm this second component, we do observe a higher number of GCs in this galaxy.
100. *VCC 1993.* GCs are rarely detected. The GC number density peak is offset from the galaxy center. $N_{\rm GC}$ from the ACSVCS (E. W. Peng et al. 2008) is negative, but we have a positive number. Please check Section 3.2.
101. *NGC 4660.* It has a neighbor, NGC 4649, so we fit two Sérsic functions simultaneously. $R_{e,gc}$ from the previous study ($R_{e,gc} = 0\farcm7 \pm 0\farcm1$, T. Carleton et al. 2019) is much smaller than our result, and $N_{\rm GC}$ from the ACSVCS (E. W. Peng et al. 2008) is also smaller than that in this study. It may be due to the limited spatial coverage of previous studies. Please check Section 3.2.
102. *IC 3735.* There is no special feature in GC properties. The $N_{\rm GC}$ from the ACSVCS (E. W. Peng et al. 2008) is consistent with that in this study.
103. *IC 3773.* There is no special feature in GC properties. The $N_{\rm GC}$ from the ACSVCS (E. W. Peng et al. 2008) is consistent with that in this study.
104. *IC 3779.* There is no special feature in GC properties. The $N_{\rm GC}$ of this galaxy in the ACSVCS (E. W. Peng et al. 2008) is slightly smaller than our result, but they are consistent within the margin of error.
105. *NGC 4694.* The red GC population is larger than the blue GC population.
106. *NGC 4710.* This galaxy is on the edge of the NGVS footprint. A. Maybhate et al. (2010) detected 63 GC candidates using HST/ACS image.
107. *NGC 4733.* The GC number density peak is a little offset from the galaxy center.
108. *NGC 4754.* There is a neighbor galaxy in the east, so we masked it out. The blue and red GC populations are comparable. The $N_{\rm GC}$ from previous studies ($N_{\rm GC} = 115 \pm 15$, J. R. Hargis & K. L. Rhode 2012; $N_{\rm GC} = 103 \pm 17$, E. W. Peng et al. 2008) are slightly smaller than our result, but they are consistent within the margin of error. The $R_{e,gc}$ from previous studies ($R_{e,gc} = 2\farcm6 \pm 0\farcm9$, J. R. Hargis & K. L. Rhode 2012; T. Carleton et al. 2019) is larger than that in this study.
109. *NGC 4762.* There is a neighbor galaxy in the east, so we masked it out. This galaxy is on the edge of the NGVS footprint. The $N_{\rm GC}$ from previous studies ($N_{\rm GC} = 270 \pm 30$, J. R. Hargis & K. L. Rhode 2012; $N_{\rm GC} = 211 \pm 34$, E. W. Peng et al. 2008) are slightly smaller than our result, but they are consistent within the margin of error. The $R_{e,gc}$ from previous studies ($R_{e,gc} = 1\farcm4 \pm 0\farcm4$, J. R. Hargis & K. L. Rhode 2012; T. Carleton et al. 2019) is consistent with that in this study.
110. *NGC 5839.* It has a neighbor, NGC 5846, so we fit two Sérsic functions simultaneously.
111. *NGC 5846.* It has a neighbor, NGC 5839, so we fit two Sérsic functions simultaneously. The blue and red GC populations are comparable. D. A. Forbes et al. (1997) studied the GC system of this galaxy based on the HST/WFPC2 observation, and they provided $N_{\rm GC} = 4670$

based on the extrapolation. This value is much larger than our result, and it could be due to the limited spatial coverage and extrapolation of the previous study. Interestingly, D. A. Forbes et al. (1997) estimated S_N to be 4.1 ± 1.1, which is much smaller than our result even with larger N_{GC}. This discrepancy is mainly due to the different magnitudes of the host galaxy.

112. *NGC 5866.* GCs are more centrally concentrated than other galaxies. There are several previous studies on the GC system of this galaxy (M. Cantiello et al. 2007; J. R. Hargis & K. L. Rhode 2012), and the N_{GC} of the previous studies (N_{GC} ~ 300, M. Cantiello et al. 2007; $N_{GC} = 340 \pm 80$, J. R. Hargis & K. L. Rhode 2012) are consistent with our result. $R_{e,gc}$ was also estimated in previous studies ($R_{e,gc} = 3\farcm1 \pm 0\farcm7$, J. R. Hargis & K. L. Rhode 2012; J. P. Caso et al. 2019), but the value from the literature is much larger than that in this study.
113. *PGC 058114.* The GC number density peak is offset from the galaxy center.
114. *NGC 6548.* It contains only one GC within $2R_{e,gc}$.
115. *NGC 7280.* It contains no GC within $2R_{e,gc}$.
116. *NGC 7332.* There is no special feature in GC properties. N_{GC} from previous studies ($N_{GC} = 190 \pm 30$, D. A. Forbes et al. 2001; $N_{GC} = 175 \pm 15$, M. D. Young et al. 2012) are larger than that in this study, but they are consistent within the margin of error. $R_{e,gc}$ from the previous study (M. J. Hudson & B. Robison 2018) is consistent with that of this study.
117. *NGC 7457.* There is no special feature in GC properties. N_{GC} from the previous study ($N_{GC} = 210 \pm 30$, J. R. Hargis et al. 2011) is larger than that in this study, but they are consistent within the margin of error.
118. *NGC 7454.* GCs are more centrally concentrated than other galaxies.

ORCID iDs

Sungsoon Lim https://orcid.org/0000-0002-5049-4390
Eric W. Peng https://orcid.org/0000-0002-2073-2781
Patrick Côté https://orcid.org/0000-0003-1184-8114
Laura Ferrarese https://orcid.org/0000-0002-8224-1128
Joel C. Roediger https://orcid.org/0000-0002-0363-4266
Chengze Liu https://orcid.org/0000-0002-4718-3428
Chelsea Spengler https://orcid.org/0000-0002-1685-4284
Elisabeth Sola https://orcid.org/0000-0002-2814-3578
Pierre-Alain Duc https://orcid.org/0000-0003-3343-6284
Laura V. Sales https://orcid.org/0000-0002-3790-720X
John P. Blakeslee https://orcid.org/0000-0002-5213-3548
Jean-Charles Cuillandre https://orcid.org/0000-0002-3263-8645
Patrick R. Durrell https://orcid.org/0000-0001-9427-3373
Eric Emsellem https://orcid.org/0000-0002-6155-7166
Stephen D. J. Gwyn https://orcid.org/0000-0001-8221-8406
Ariane Lançon https://orcid.org/0000-0002-7214-8296
Francine R. Marleau https://orcid.org/0000-0002-1442-2947
J. Christopher Mihos https://orcid.org/0000-0002-7089-8616
Oliver Müller https://orcid.org/0000-0003-4552-9808
Thomas H. Puzia https://orcid.org/0000-0003-0350-7061
Rubén Sánchez-Janssen https://orcid.org/0000-0003-4945-0056

References

Akhil, K. R., Kartha, S. S., & Mathew, B. 2024, MNRAS, 530, 2907
Alamo-Martìnez, K. A., & Blakeslee, J. P. 2017, ApJ, 849, 6
Alamo-Martìnez, K. A., Chies-Santos, A. L., Beasley, M. A., et al. 2021, MNRAS, 503, 2406
Astropy Collaboration, Price-Whelan, A. M., Lim, P. L., et al. 2022, ApJ, 935, 167
Astropy Collaboration, Price-Whelan, A. M., Sipőcz, B. M., et al. 2018, AJ, 156, 123
Astropy Collaboration, Robitaille, T. P., Tollerud, E. J., et al. 2013, A&A, 558, A33
Beasley, M. A., Forbes, D. A., Brodie, J. P., & Kissler-Patig, M. 2004, MNRAS, 347, 1150
Bertin, E., & Arnouts, S. 1996, A&AS, 117, 393
Bìlek, M., Duc, P.-A., Cuillandre, J.-C., et al. 2020, MNRAS, 498, 2138
Blakeslee, J. P., Jordán, A., Mei, S., et al. 2009, ApJ, 694, 556
Blakeslee, J. P., Tonry, J. L., & Metzger, M. R. 1997, AJ, 114, 482
Blom, C., Forbes, D. A., Foster, C., Romanowsky, A. J., & Brodie, J. P. 2014, MNRAS, 439, 2420
Blom, C., Spitler, L. R., & Forbes, D. A. 2012, MNRAS, 420, 37
Boulade, O., Charlot, X., & Abbon, P. 2003, Proc. SPIE, 4841, 72
Brodie, J. P., Strader, J., Denicoló, G., et al. 2005, AJ, 129, 2643
Brodie, J. P., Romanowsky, A. J., Strader, J., et al. 2014, ApJ, 796, 52
Cantiello, M., Blakeslee, J. P., & Raimondo, G. 2007, ApJ, 668, 209
Cappellari, M., Emsellem, E., Krajnović, D., et al. 2011, MNRAS, 413, 813
Cappellari, M., McDermid, R. M., Alatalo, K., et al. 2013, MNRAS, 432, 1862
Carleton, T., Errani, R., Cooper, M., et al. 2019, MNRAS, 485, 382
Caso, J. P., De Bórtoli, B. J., Ennis, A. I., & Bassino, L. P. 2019, MNRAS, 488, 4504
Chies-Santos, A. L., Larsen, S. S., Wehner, E. M., et al. 2011, A&A, 525, A19
Ciotti, L., & Bertin, G. 1999, A&A, 352, 447
Côté, P., Blakeslee, J. P., Ferrarese, L., et al. 2004, ApJS, 153, 223
Côté, P., McLaughlin, D. E., Cohen, J. G., & Blakeslee, J. P. 2003, ApJ, 591, 850
De Bórtoli, B. J., Caso, J. P., Ennis, A. I., & Bassino, L. P. 2022, MNRAS, 510, 5725
de Brito Silva, D., Coelho, P., Cortesi, A., et al. 2022, A&A, 664, A129
Duc, P.-A. 2020, arXiv:2007.13874
Duc, P.-A., Cuillandre, J.-C., Karabal, E., et al. 2015, MNRAS, 446, 120
Durrell, P. R., Côté, P., Peng, E. W., et al. 2014, ApJ, 794, 103
Durrell, P. R., Harris, W. E., Geisler, D., & Pudritz, R. E. 1996, AJ, 112, 972
Ferrarese, L., Côté, P., Cuillandre, J.-C., et al. 2012, ApJS, 200, 4
Ferrarese, L., Côté, P., MacArthur, L. A., et al. 2020, ApJ, 890, 128
Forbes, D. A. 1996, AJ, 112, 954
Forbes, D. A. 2017, MNRAS, 472, L104
Forbes, D. A., Brodie, J. P., & Huchra, J. 1997, AJ, 113, 887
Forbes, D. A., Georgakakis, A. E., & Brodie, J. P. 2001, MNRAS, 325, 1431
Forbes, D. A., Faifer, F. R., Forte, J. C., et al. 2004, MNRAS, 355, 608
Foreman-Mackey, D., Hogg, D. W., Lang, D., & Goodman, J. 2013, PASP, 125, 306
Georgiev, I. Y., Puzia, T. H., Hilker, M., & Goudfrooij, P. 2009, MNRAS, 392, 879
Gómez, M., & Richtler, T. 2004, A&A, 415, 499
Gwyn, S. D. J. 2008, PASP, 120, 212
Hargis, J. R., & Rhode, K. L. 2012, AJ, 144, 164
Hargis, J. R., & Rhode, K. L. 2014, ApJ, 796, 62
Hargis, J. R., Rhode, K. L., Strader, J., & Brodie, J. P. 2011, ApJ, 738, 113
Harris, W. E. 2001, in Swiss Society for Astrophysics and Astronomy, Star Clusters, Saas-Fee Advanced Course 28, ed. L. Labhardt & B. Binggeli (Berlin: Springer), 223
Harris, W. E. 2009, ApJ, 703, 939
Harris, W. E. 2023, ApJS, 265, 9
Harris, W. E., Blakeslee, J. P., & Harris, G. L. H. 2017, ApJ, 836, 67
Harris, W. E., Morningstar, W., Gnedin, O. Y., et al. 2014, ApJ, 797, 128
Hartman, K., Harris, W. E., Blakeslee, J. P., Ma, C.-P., & Greene, J. E. 2023, ApJ, 953, 154
Hudson, M. J., & Robison, B. 2018, MNRAS, 477, 3869
Jordán, A., Blakeslee, J. P., Côté, P., et al. 2007a, ApJS, 169, 213
Jordán, A., McLaughlin, D. E., Côté, P., et al. 2007b, ApJS, 171, 101
Kartha, S. S., Forbes, D. A., Alabi, A. B., et al. 2016, MNRAS, 458, 105
Kartha, S. S., Forbes, D. A., Spitler, L. R., et al. 2014, MNRAS, 437, 273
Kundu, A., & Whitmore, B. C. 2001a, AJ, 122, 1251
Kundu, A., & Whitmore, B. C. 2001b, AJ, 121, 2950
Kundu, A., Zepf, S. E., Hempel, M., et al. 2005, ApJL, 634, L41
Lambert, R. A., Rhode, K. L., & Vesperini, E. 2020, ApJ, 900, 45

Larsen, S. S., & Brodie, J. P. 2000, AJ, 120, 2938
Larsen, S. S., Brodie, J. P., Huchra, J. P., Forbes, D. A., & Grillmair, C. J. 2001, AJ, 121, 2974
Lee, M. G. 2003, JKAS, 36, 189
Lee, M. G., Kim, E., & Geisler, D. 1998, AJ, 115, 947
Lee, M. G., Park, H. S., & Hwang, H. S. 2010, Sci, 328, 334
Lee, M. G., Park, H. S., Kim, E., et al. 2008, ApJ, 682, 135
Lim, S., Côté, P., Peng, E. W., et al. 2020, ApJ, 899, 69
Lim, S., Peng, E. W., Côté, P., et al. 2018, ApJ, 862, 82
Lim, S., Peng, E. W., Côté, P., et al. 2024, ApJ, 966, 168
Lim, S., Peng, E. W., Duc, P.-A., et al. 2017, ApJ, 835, 123
Liu, C., Peng, E. W., Toloba, E., et al. 2015, ApJL, 812, L2
Maybhate, A., Goudfrooij, P., Chandar, R., & Puzia, T. H. 2010, ApJ, 721, 893
McLaughlin, D. E. 1999, AJ, 117, 2398
Mei, S., Blakeslee, J. P., Côté, P., et al. 2007, ApJ, 655, 144
Miller, B. W., & Lotz, J. M. 2007, ApJ, 670, 1074
Muratov, A. L., & Gnedin, O. Y. 2010, ApJ, 718, 1266
Peng, E. W., Jordán, A., Côté, P., et al. 2006, ApJ, 639, 95
Peng, E. W., Jordán, A., Côté, P., et al. 2008, ApJ, 681, 197
Peng, E. W., Ferguson, H. C., Goudfrooij, P., et al. 2011, ApJ, 730, 23
Prole, D. J., Hilker, M., van der Burg, R. F. J., et al. 2019, MNRAS, 484, 4865
Puzia, T. H., Zepf, S. E., Kissler-Patig, M., et al. 2002, A&A, 391, 453
Rhode, K. L. 2012, AJ, 144, 154
Rhode, K. L., & Zepf, S. E. 2001, AJ, 121, 210
Rhode, K. L., & Zepf, S. E. 2004, AJ, 127, 302
Rhode, K. L., Zepf, S. E., Kundu, A., & Larner, A. N. 2007, AJ, 134, 1403
Spitler, L. R., & Forbes, D. A. 2009, MNRAS, 392, L1
Sola, E., Duc, P.-A., Richards, F., et al. 2022, A&A, 662, A124
Spitler, L. R., Forbes, D. A., Strader, J., Brodie, J. P., & Gallagher, J. S. 2008, MNRAS, 385, 361
Tamura, N., Sharples, R. M., Arimoto, N., et al. 2006, MNRAS, 373, 588
Usher, C., Forbes, D. A., Spitler, L. R., et al. 2013, MNRAS, 436, 1172
van Dokkum, P., Cohen, Y., Danieli, S., et al. 2018, ApJL, 856, L30
Villegas, D., Jordán, A., Peng, E. W., et al. 2010, ApJ, 717, 603
Young, M. D., Dowell, J. L., & Rhode, K. L. 2012, AJ, 144, 103
Zaritsky, D., Aravena, M., Athanassoula, E., et al. 2015, ApJ, 799, 159